



Calhoun: The NPS Institutional Archive
DSpace Repository

NPS Scholarship

Theses

1987

Numerical simulations of the California
Current: filament formation as related to
baroclinic instability.

Olivier, David A.

<https://hdl.handle.net/10945/22835>

Downloaded from NPS Archive: Calhoun



Calhoun is the Naval Postgraduate School's public access digital repository for research materials and institutional publications created by the NPS community. Calhoun is named for Professor of Mathematics Guy K. Calhoun, NPS's first appointed -- and published -- scholarly author.

Dudley Knox Library / Naval Postgraduate School
411 Dyer Road / 1 University Circle
Monterey, California USA 93943

<http://www.nps.edu/library>



DUDLEY KNOX LIBRARY
NAVAL POSTGRADUATE SCHOOL
MONTEREY, CALIFORNIA 93943-5002

NAVAL POSTGRADUATE SCHOOL

Monterey, California



THESIS

NUMERICAL SIMULATIONS OF THE CALIFORNIA
CURRENT:
FILAMENT FORMATION AS RELATED TO
BAROCLINIC INSTABILITY

by

David A. Olivier

September 1987

Thesis Advisor

D. C. Smith IV

Approved for public release; distribution is unlimited.

T234313

REPORT DOCUMENTATION PAGE

1a REPORT SECURITY CLASSIFICATION UNCLASSIFIED		1b RESTRICTIVE MARKINGS	
2a SECURITY CLASSIFICATION AUTHORITY		3 DISTRIBUTION/AVAILABILITY OF REPORT Approved for public release, distribution is unlimited	
2b DECLASSIFICATION/DOWNGRADING SCHEDULE		5 MONITORING ORGANIZATION REPORT NUMBER(S)	
4 PERFORMING ORGANIZATION REPORT NUMBER(S)		7a NAME OF MONITORING ORGANIZATION Naval Postgraduate School	
6a NAME OF PERFORMING ORGANIZATION Naval Postgraduate School	6b OFFICE SYMBOL (if applicable) 68	7b ADDRESS (City, State, and ZIP Code) Monterey, California 93943-5000	
6c ADDRESS (City, State, and ZIP Code) Monterey, California 93943-5000		9 PROCUREMENT INSTRUMENT IDENTIFICATION NUMBER	
8a NAME OF FUNDING/SPONSORING ORGANIZATION	8b OFFICE SYMBOL (if applicable)	10 SOURCE OF FUNDING NUMBERS	
8c ADDRESS (City, State, and ZIP Code)		PROGRAM ELEMENT NO	PROJECT NO
		TASK NO	WORK UNIT ACCESSION NO
11 TITLE (Include Security Classification) NUMERICAL SIMULATIONS OF THE CALIFORNIA CURRENT: FILAMENT FORMATION AS RELATED TO BAROCLINIC INSTABILITY			
12 PERSONAL AUTHOR(S) Olivier, David A.			
13a TYPE OF REPORT Master's Thesis	13b TIME COVERED FROM _____ TO _____	14 DATE OF REPORT (Year Month Day) 1987 September	15 PAGE COUNT 70
16 SUPPLEMENTARY NOTATION			
17 COSATI CODES		18 SUBJECT TERMS (Continue on reverse if necessary and identify by block number)	
FIELD	GROUP	PE ocean model, filaments, coastal jet, instability, baroclinic, barotropic, topography, eddies, friction, non-linear	
19 ABSTRACT (Continue on reverse if necessary and identify by block number)			
<p>Offshore jets or filaments are a well observed phenomenon in the California Current System. Their surface and subsurface structures as well as their spatial and temporal variability are well documented. The methods by which these filaments are formed is not as well understood as their structural form. The most common generation theories are: (1) variations in wind stress coupled with topographic irregularities, (2) dynamic instability and (3) geostrophic turbulence. In this study an attempt is made to identify the factor(s) responsible for filament formation south of Cape Mendocino by numerically simulating the California Current System using a two-layer, non-linear, primitive equation model. It is shown that baroclinic instability is the primary method by which filaments are formed in this region and that other factors such as barotropic instability, friction and non-linearities can alter the characteristics of the fastest growing baroclinically unstable wave.</p>			
20 DISTRIBUTION/AVAILABILITY OF ABSTRACT <input checked="" type="checkbox"/> UNCLASSIFIED/UNLIMITED <input type="checkbox"/> SAME AS RPT <input type="checkbox"/> DTIC USERS		21 ABSTRACT SECURITY CLASSIFICATION UNCLASSIFIED	
22a NAME OF RESPONSIBLE INDIVIDUAL David C. Smith, IV		22b TELEPHONE (Include Area Code) 408-646-3350	22c OFFICE SYMBOL 68Si

Approved for public release; distribution is unlimited.

Numerical Simulations of the California Current:
Filament Formation as Related to Baroclinic Instability

by

David A. Olivier
Lieutenant, United States Navy
B.S., University of Virginia, 1980

Submitted in partial fulfillment of the
requirements for the degree of

MASTER OF SCIENCE IN METEOROLOGY AND OCEANOGRAPHY

from the

NAVAL POSTGRADUATE SCHOOL
September 1987

ABSTRACT

Offshore jets or filaments are a well observed phenomenon in the California Current System. Their surface and subsurface structures as well as their spatial and temporal variability are well documented. The methods by which these filaments are formed is not as well understood as their structural form. The most common generation theories are: (1) variations in wind stress coupled with topographic irregularities, (2) dynamic instability and (3) geostrophic turbulence. In this study an attempt is made to identify the factor(s) responsible for filament formation south of Cape Mendocino by numerically simulating the California Current System using a two-layer, non-linear, primitive equation model. It is shown that baroclinic instability is the primary method by which filaments are formed in this region and that other factors such as barotropic instability, friction and non-linearities can alter the characteristics of the fastest growing baroclinically unstable wave.

Handwritten notes at the top right of the page, including the number '0167' and other illegible scribbles.

TABLE OF CONTENTS

I.	INTRODUCTION	9
A.	THE CALIFORNIA CURRENT SYSTEM	9
B.	FILAMENTS IN THE CALIFORNIA CURRENT SYSTEM	9
C.	FILAMENT FORMATION	10
D.	PURPOSE OF THIS STUDY	11
II.	NUMERICAL SIMULATION OF THE CALIFORNIA CURRENT	13
A.	THE NUMERICAL MODEL	13
1.	Model Equations	13
2.	Model Domain	13
3.	Boundary Conditions	15
B.	NUMERICAL EXPERIMENTS	15
1.	The Reference State	15
2.	Variation of Parameters	21
III.	BAROCLINIC ANALYSIS	40
A.	SETTING UP THE LINEAR INSTABILITY PROBLEM	40
1.	Instability of a Non-Zonal Flow	40
2.	Critical Velocity and Growth Rate	44
B.	APPLICATION OF ANALYTIC RESULTS TO MODEL OUTPUT	50
C.	FURTHER ASPECTS OF THE INSTABILITY PROBLEM	55
1.	Effects of Friction	56
2.	Non-linear Instability Effects	57
3.	Mixed Instability Effects	58
4.	Baroclinic Instability with Complex Wavenumbers	58

IV.	DISCUSSION AND CONCLUSIONS	60
A.	ANALYSIS OF RESULTS	60
	1. Comparison of Results with Observational Data	60
	2. The Filament Formation Process	60
B.	IMPORTANCE OF RESULTS	61
C.	RECOMMENDATIONS FOR FUTURE STUDIES	62
D.	CONCLUSIONS	62
	APPENDIX: SYMBOLS AND NOTATION	63
	LIST OF REFERENCES	65
	INITIAL DISTRIBUTION LIST	67

LIST OF TABLES

1. REFERENCE STATE MODEL PARAMETERS	20
2. VARIATION OF MODEL PARAMETERS	24
3. WAVE PARAMETERS FROM MODEL OUTPUT FIELDS ($\alpha = 270^\circ$)	50
4. WAVE PARAMETERS FROM MODEL OUTPUT FIELDS ($\alpha = 300^\circ$)	51
5. FILAMENT CHARACTERISTICS, OBSERVED VS. MODELED	60

LIST OF FIGURES

1.1	Seasonal Configurations of the California Current System (Ikeda and Emery, 1984)	9
1.2	Surface Velocity Field of a Filament (Flament <i>et al.</i> , 1985)	11
2.1	Geographical Positioning of Model Domain	14
2.2	Actual Topography in Vicinity of Mendocino Escarpment (Chen, 1986)	16
2.3	Smoothed Topography used in Numerical Simulations	17
2.4	Reference State Flows and Topography	19
2.5	Model Output Fields of Height Anomalies for Reference State	22
2.6	Model Output Fields of Upper Layer Velocity for Reference State	23
2.7	Experiment # 1 (H_1 Increased to 250 m) Model Output Height Anomalies	25
2.8	Experiment # 2 (Eddy Removed) Model Output Height Anomalies	26
2.9	Experiment # 3 (Jet Moved Farther Offshore) Model Output Height Anomalies	28
2.10	Experiment # 4 (Topography Removed) Model Output Height Anomalies	29
2.11	Experiment # 5 (Increased Lower Layer Velocity) Model Output Height Anomalies	30
2.12	Experiment # 6 (Lower Layer Flow Direction Reversed) Model Output Height Anomalies	31
2.13	Experiment # 7 (Zonal Flow Westward) Model Output Height Anomalies	33
2.14	Experiment # 8 (Zonal Flow Eastward) Model Output Height Anomalies	34
2.15	Experiment # 9 (Eddy and Topography Removed) Model Output Height Anomalies	35
2.16	Experiment #10 (Northwest to Southeast Flow) Model Output Height Anomalies	37
2.17	Experiment #11 (V_{1j} Reduced to 0.2 m/s) Model Output Height Anomalies	38

2.18	Experiment #12 (V_{1j} Reduced to 0.1 m/s) Model Output Height Anomalies	39
3.1	Coordinate System Orientation	43
3.2	Marginal Stability Curves for $\alpha = 270^\circ$	46
3.3	Marginal Stability Curves for $\alpha = 300^\circ$	47
3.4	Growth Rates for $\alpha = 270^\circ$	48
3.5	Growth Rates for $\alpha = 300^\circ$	49
3.6	Marginal Stability Curves for Model Output Wave Characteristics	52
3.7	Growth Rate Positions of Model Output Waves for Shear Velocity of 0.4 m/s	53
3.8	Reference State Wave Amplitude Growth	54
3.9	Growth Rate Variations of Reference State Waves	55
3.10	Marginal Stability Curves for Zonal Flow	56
3.11	Spatial and Temporal Wave Growth of Gulf Stream Meanders (Watts and Johns, 1982)	59

I. INTRODUCTION

A. THE CALIFORNIA CURRENT SYSTEM

The California Current System, CCS, has been extensively studied by Hickey (1979). The CCS consists of four separate currents that are spatially and seasonally distributed off the West Coast of the United States. They are: (1) the California Current, a southward flowing surface jet; (2) the California Undercurrent, a northward flowing sub-surface jet; (3) the Davidson Current, a poleward flowing surface jet north of Point Conception; and (4) the Southern California Countercurrent, a northward flowing surface current south of Point Conception in the California Bight (Hickey, 1979). Figure 1.1 shows the average seasonal configurations from Ikeda and Emery (1984) for the CCS. Typical surface jet velocities are on the order of 20 to 40 cm/s. The California Undercurrent has a typical strength of about 5-10 cm/s. For the profiles on the left, where the California Undercurrent is present, the surface jet depth is about 150 m while for the profiles without a subsurface jet, the surface jet extends down to about 300 m.

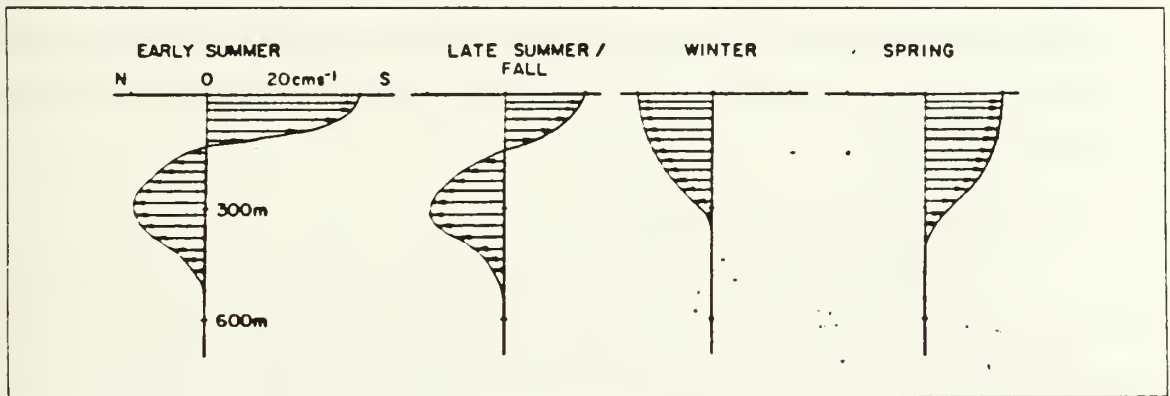


Figure 1.1 Seasonal Configurations of the California Current System (Ikeda and Emery, 1984).

B. FILAMENTS IN THE CALIFORNIA CURRENT SYSTEM

The presence of offshore jets or filaments in the CCS is well documented. Satellite radiometry and color scanning along with intensive *in situ* data such as that

obtained during the Coastal Ocean Dynamics Experiment (CODE) have provided large data bases for these features.

From an observational standpoint, filaments are well documented. Definitive studies by Flament *et al.* (1985), Kosro (1987) and Kosro and Huyer (1986), for example, have greatly expanded our knowledge of filament surface and subsurface structures along with their spatial and temporal variability.

Filaments consist of strong baroclinic jets flowing offshore at peak velocities of 0.5 m/s or greater (Rienecker *et al.*, 1985), with narrow return flows to the south (Flament *et al.*, 1985). The offshore extent of filaments is typically on the order of 200 to 300 km with maxima of around 500 km (Brink and Hartwig, 1985). Filaments advect cold upwelled coastal waters away from the continental shelf.

Filament widths are on the order of 50 km (Flament *et al.*, 1985). The wavelength associated with their occurrence at numerous points along the coast is roughly 100 to 400 km for the region to the north of Cape Mendocino (Ikeda and Emery, 1984). Formation time scales are generally on the order of weeks with lifetimes on the order of a month. Figure 1.2 shows the surface velocity field derived from satellite feature tracking for a filament studied by Flament *et al.* (1985).

Filaments are seasonal in nature. Few have been observed during late winter through early spring. Their first appearance is off the Baja Peninsula in March. Between April and May they occur between Point Conception and Cape Mendocino and by late summer they reach their maximum northward extent off the Oregon coast. Generally, filaments have been more observed south of Cape Mendocino. (Brink and Hartwig, 1985)

C. FILAMENT FORMATION

The precise formation process for filaments is not as well understood as their characteristics once formed. Numerous theories abound with the most prevalent causative forces being: (1) coastally linked processes associated with variations in wind stress coupled with irregularities in the alongshore topography, (2) dynamical instabilities of the CCS, and (3) geostrophic mesoscale eddy field interactions with the CCS. It is possible and indeed probable that more than one theory may be responsible for filament formation.

Ikeda and Emery (1984) demonstrated by a combination of observational data and numerical experiments that coastal irregularities off the coast of Northern California and Oregon are strongly correlated with filament formation. They also

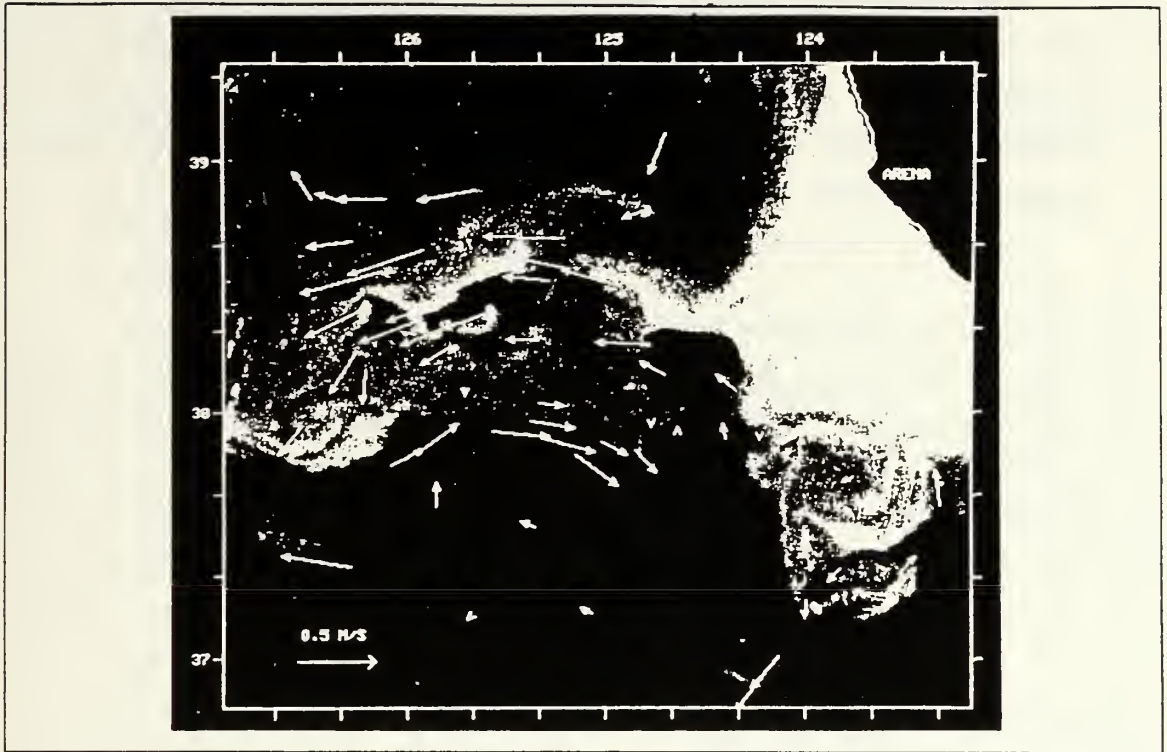


Figure 1.2 Surface Velocity Field of a Filament (Flament *et al.*, 1985).

showed that baroclinic instability was probably the primary causative force north of Cape Mendocino. Batteen (1987) demonstrated that baroclinic instability could occur in the CCS due to imposing an unstable jet profile similar to the early summer profile shown in Figure 1.1. Chen (1986) showed that baroclinic instability coupled with topographic variations are important to the destabilization of the CCS in the vicinity of Cape Mendocino. Mysak (1977) also demonstrated the importance of baroclinic instability in a numerical study of the CCS off Vancouver Island. Mooers and Robinson (1984) documented an eddy pair off Northern California, while Owen (1980) and Huyer *et al.* (1984) observed strong eddy-like features in the northeastern Pacific close to the continental slope.

D. PURPOSE OF THIS STUDY

The objective of this study is to determine the causative factor(s) involved with filament formation along the coast of California south of Cape Mendocino. A two-layer, non-linear, primitive equation model with topography is used to simulate the dynamics of the CCS. The results strongly point to baroclinic instability as the primary generation mechanism for filaments in this region.

The specifics of the model and the various numerical experiments are covered in Chapter II. The linear baroclinic instability problem is formulated in Chapter III and the results applied to the data from the numerical experiments to verify the claim of baroclinic instability to the CCS. In Chapter IV, the results are discussed and conclusions presented.

II. NUMERICAL SIMULATION OF THE CALIFORNIA CURRENT

A. THE NUMERICAL MODEL

1. Model Equations

Simulation of the CCS is performed using a two-layer, primitive equation, semi-implicit numerical scheme initially developed by Hurlburt (1974). This scheme has been employed in numerous ocean mesoscale circulation studies (e.g., Hurlburt and Thompson, 1980, 1982; Smith and O'Brien, 1983; and Smith, 1986). Linear test cases have been run for comparison with linear analytic solutions to show that this approach is valid (Smith and Reid, 1982). Motion in each layer is governed by a momentum equation (2.1) and a continuity equation (2.2).

$$\frac{\partial \mathbf{V}_i}{\partial t} + (\nabla \cdot \mathbf{V}_i + \mathbf{V}_i \cdot \nabla) \mathbf{V}_i + \mathbf{k} \times f \mathbf{V}_i = -h_i \nabla P_i + A_h \nabla^2 \mathbf{V}_i \quad (2.1)$$

$$\frac{\partial h_i}{\partial t} + \nabla \cdot \mathbf{V}_i = 0 \quad (2.2)$$

Where i = layer index ($i=1$ upper, $i=2$ lower)

Variables and notation are defined in the Appendix. The fluid is assumed to be hydrostatic and Boussinesq. The density in each layer is constant. The effects of winds, tides, thermodynamics and thermohaline mixing are not included.

2. Model Domain

A rectangular region (1100 km \times 800 km) was divided into 10 km by 10 km squares to form the grid for the numerical model finite differencing. By rotating the grid through a desired angle, the model can be used to simulate the flow within the CCS as indicated by Figure 2.1.

Topography is included by approximating the major features apparent in the Mendocino Escarpment region. Figure 2.2 shows the digitized topography in the vicinity of the Mendocino Escarpment (Chen, 1986) and Figure 2.3 shows the topography used in the model. Principal features of the topography used in the model are: (1) a shelf region of 500 m depth extending out 50 km from the coastline which is

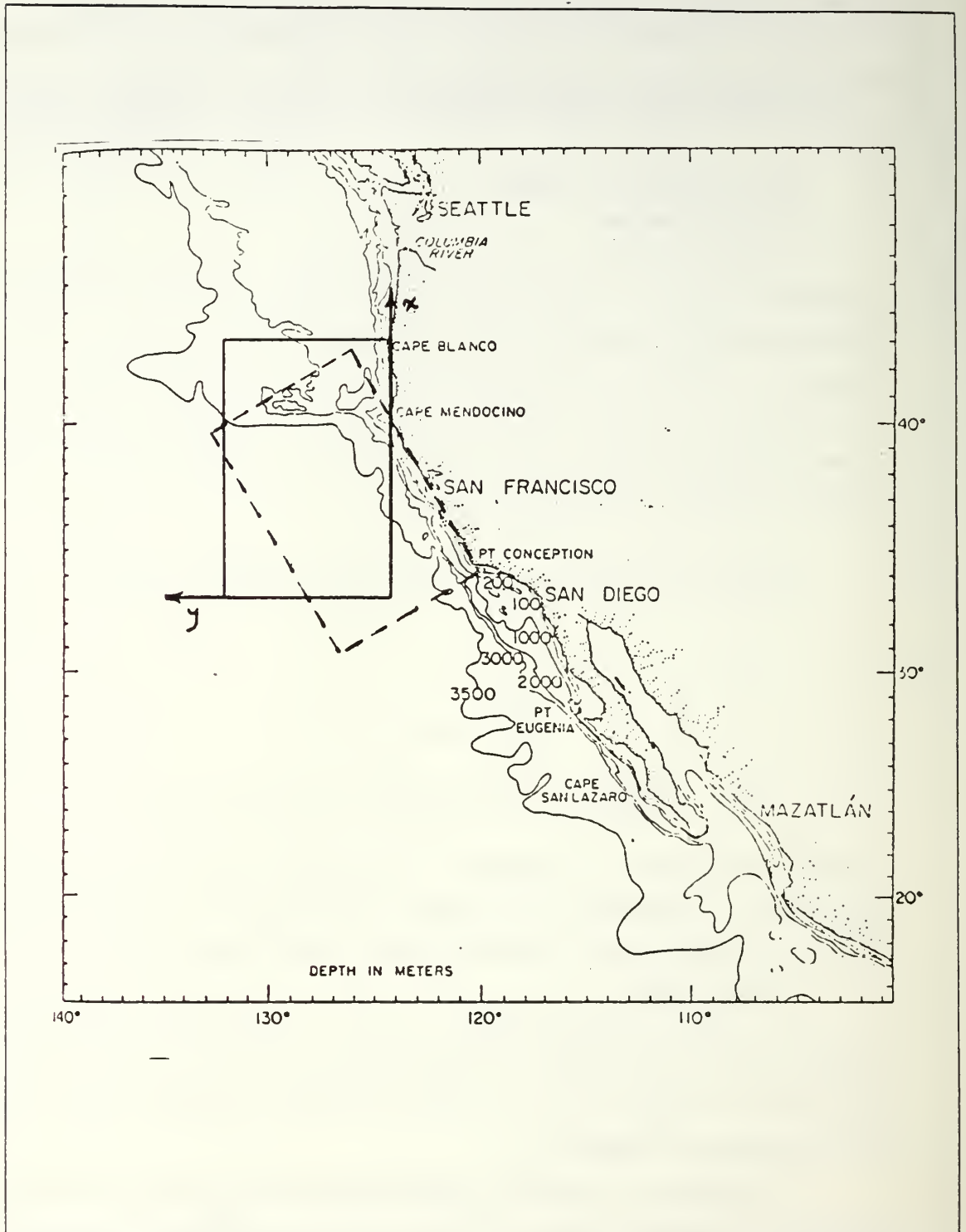


Figure 2.1 Geographical Positioning of Model Domain.

Solid box represents a basin rotation (γ) of 90° , dashed box for rotation of 120° .

a uniform vertical wall; (2) a shelf slope region extending from 50 km to ~ 100 km with an exponentially decreasing slope; (3) a modeled Mendocino Escarpment (without a ridge) which separates a 3000 m depth region to the north from 4500 m water depth to the south. The topography rotates with the model domain.

3. Boundary Conditions

Using the orientation of Figure 2.1, no-slip boundary conditions are set on the eastern and western boundaries. The northern boundary condition consists of a prescribed inflow in the upper layer. For simulated lower layer flows to the south or north the lower layer boundary consists of either a prescribed inflow or a radiation condition (Camerlengo and O'Brien, 1980) respectively. The southern boundary condition is set up just opposite the northern. The upper layer always has a radiating condition and the lower is radiating or prescribed for southward and northward lower layer flows respectively.

Obviously, these boundary conditions do not reflect totally the situation in the CCS. By putting a closed boundary to the west, there will inevitably be shear produced vorticity that is not realistic. However, it is believed that the east-west dimension of the domain is large enough so that the vorticity production at the western boundary will not affect the dynamics of the CCS which is located near the eastern boundary.

B. NUMERICAL EXPERIMENTS

1. The Reference State

In order to filter through the many possible generating mechanisms for filaments, variation of selected parameters is necessary. The problem is twofold: (1) selective variation of parameters may cause model deviations from the CCS configuration such that extrapolation of results from the model to the CCS is impossible. The results would still be important from a dynamical standpoint but without the connection with the 'real world' their usefulness is limited; (2) isolation of specific model responses by changes in model parameter(s) can be inaccurate due to complex cross correlations between varied and non-varied parameters.

In order to assess the model output variations resulting from parameter changes, a reference state is established. Instead of a simple configuration such as flat bottom barotropic flow, the reference state is selected to be as complex as possible involving such things as baroclinicity, topography and the presence of a pre-existing eddy (all suggested to be dynamically important in Chapter I). As mentioned before,

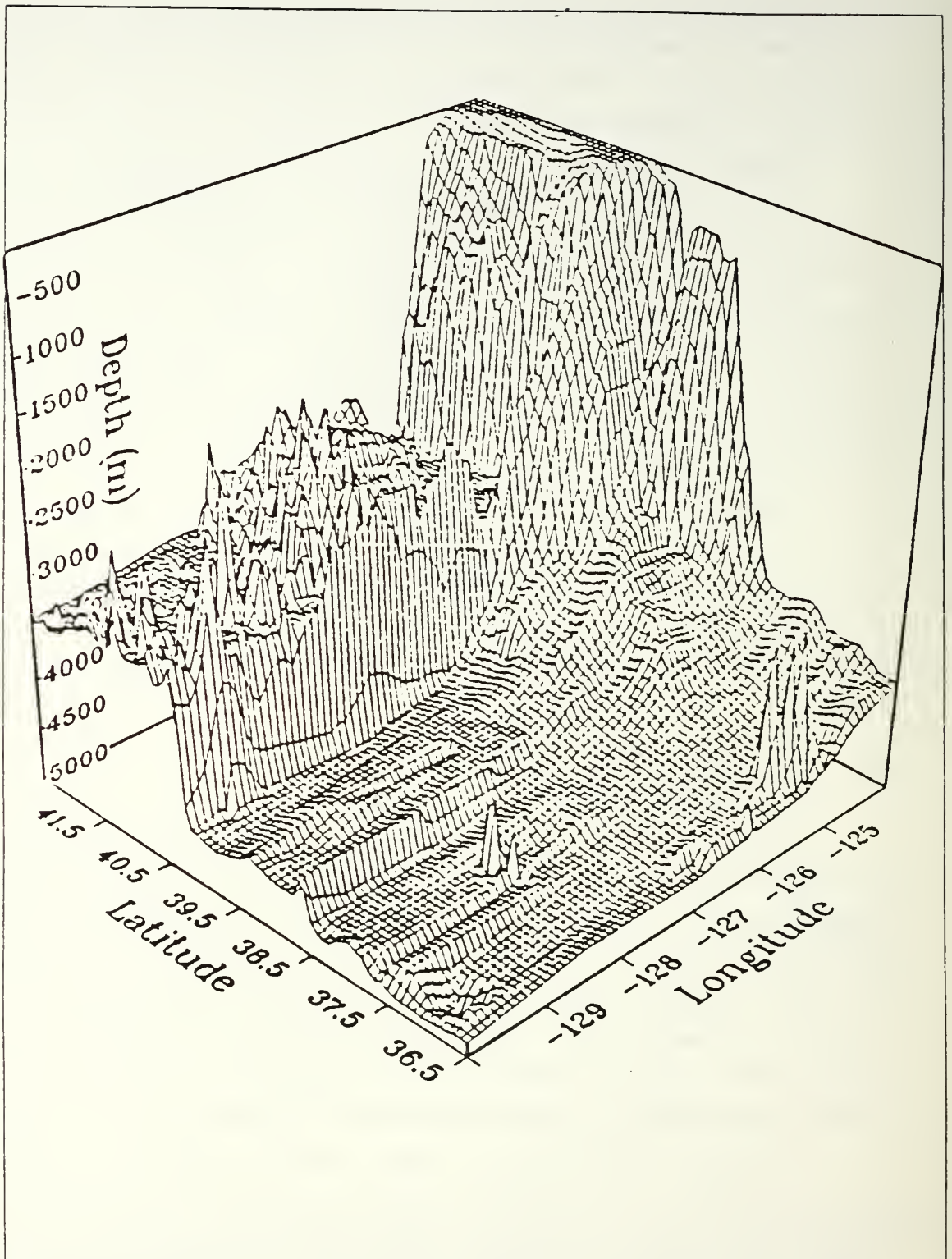


Figure 2.2 Actual Topography in Vicinity of Mendocino Escarpment (Chen, 1986).

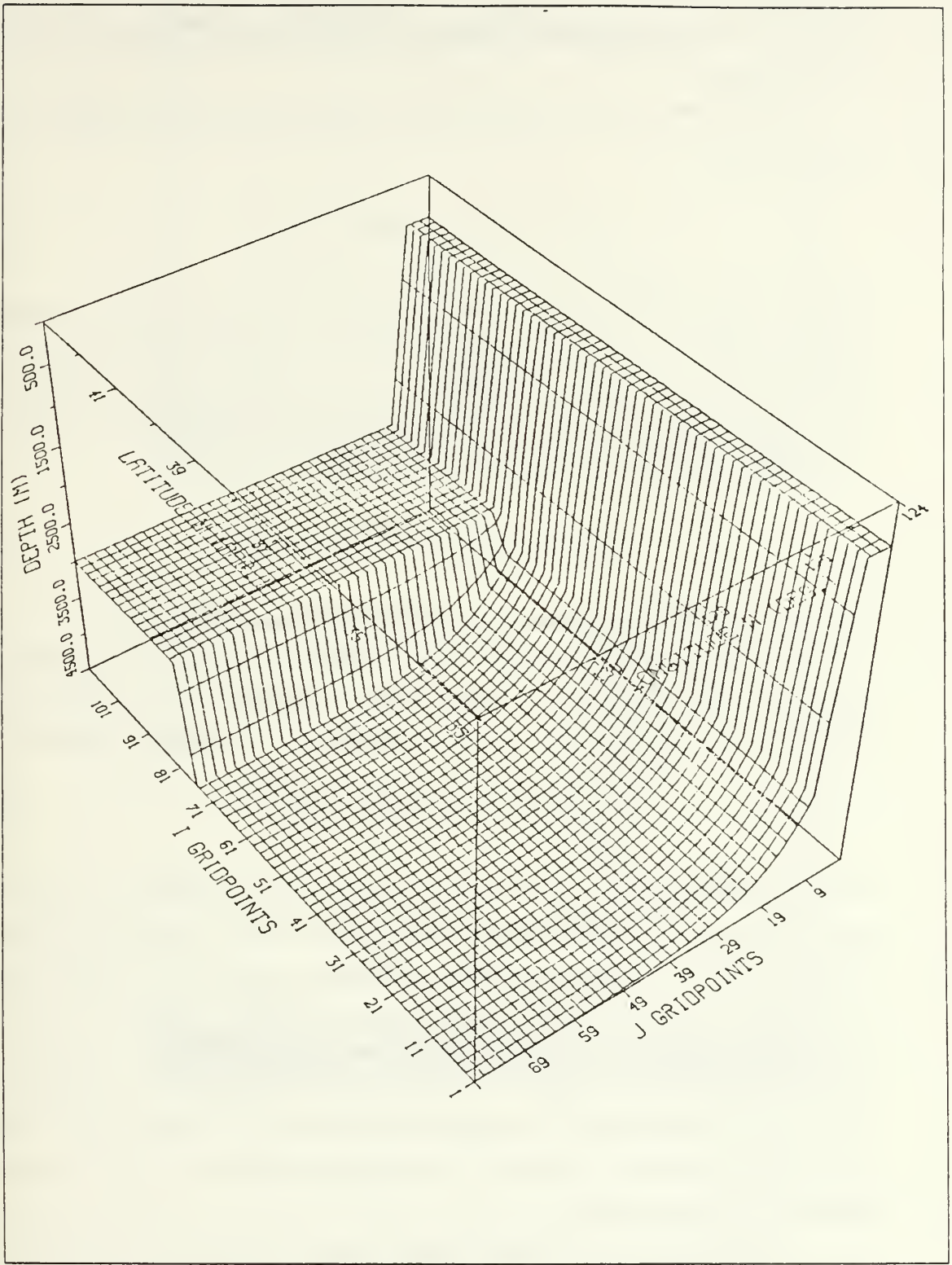


Figure 2.3 Smoothed Topography used in Numerical Simulations.

applicability of the results to the CCS is vital and use of a reference state as near as possible to the CCS configuration keeps the study focus on CCS dynamics rather than general dynamics.

The reference state consists of a two-layer geostrophically balanced, Gaussian jet of the form,

$$h_i(y) = A_i[1 - \exp(-y^2/2L^2)] \quad i = 1,2 \quad (2.3)$$

where L is the e-folding width scale of the jet and the y -axis oriented east-west as shown in Figure 2.1. The flow strength is determined by the amplitude coefficient A_i which determines the magnitude of the surface and interface height anomalies through $h_i(y)$. Additionally, a two-layer geostrophically balanced, axisymmetric, Gaussian eddy is included,

$$h_i(x,y) = A_i[1 - \exp(-R^2/2L^2)] \quad i = 1,2 \quad (2.4)$$

where $R^2 = (x^2 + y^2)$ and represents the radial distribution of the eddy.

Mean upper layer thickness is set at 150 m (H_1) which corresponds to a first internal Rossby radius, R_d , of ~ 18 km. This is comparable to the ~ 25 km R_d for the CCS (Brink and Hartwig, 1985). H_2 is dependent on the topography depth, $D(x,y)$, by,

$$H_2(x,y) = 4500 - H_1 - D(x,y) \quad (2.5)$$

The jet e-folding scale, L , is set at 25 km. The jet is fixed parallel to the coast over the slope region and the eddy positioned offshore from the jet. The spatial relationships between the jet, eddy and topography are indicated in Figure 2.4. In Figure 2.4 and in all subsequent figures of model output fields, tick marks along the x and y axis represent a distance of 275 km and 200 km respectively. The lines of constant surface height anomaly can be thought of as streamlines representing the barotropic part of the current. The interface anomaly is sloped opposite the surface with an amplitude such that its baroclinic component in the opposite direction sets up the selected flow magnitude in the lower layer.

The initial jet and eddy strength is set at 0.4 m/s (southward for jet and anticyclonic for the eddy) in the upper layer and 0.01 m/s in the same direction in the

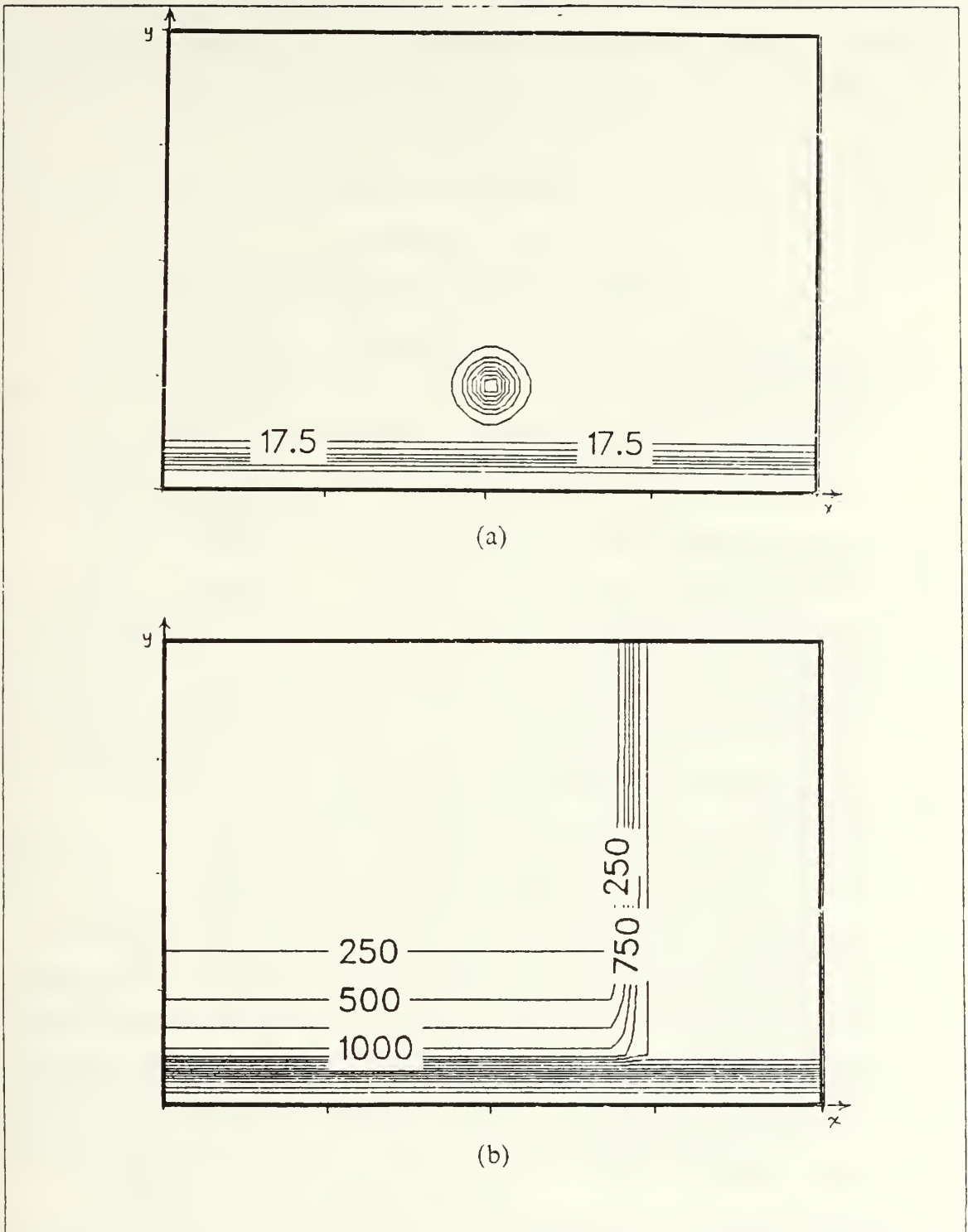


Figure 2.4 Reference State Flows and Topography.

Reference state initial conditions of (a) surface height anomaly(cm) and (b) height of bottom above 4500 m (m). Contour intervals are (a) 2.5 cm and (b) 250 m. Tick marks represent 275 km in the x direction and 200 km in the y direction.

lower layer. The horizontal Laplacian frictional coefficient, A_h , is set at $500 \text{ m}^2/\text{s}$ which is roughly in the middle of the range of A_h ($100\text{-}1000 \text{ m}^2/\text{s}$) typically used in numerical studies. A summary of model parameters for the reference state is shown in Table 1.

TABLE 1
REFERENCE STATE MODEL PARAMETERS

PARAMETER	SYMBOL	VALUE
E-W Basin Extent	L_y	800 km
N-S Basin Extent	L_x	1100 km
Initial Upper Layer Thickness	H_1	150 m
Initial Lower Layer Thickness	$H_2(x,y)$	Variable
Maximum Basin Depth	$(H_1 + H_2)_{\max}$	4500 m
Depth of Bottom	$D(x,y)$	Variable
Coriolis Parameter (@ 40° N lat.)	f_0	$0.94 \times 10^{-4} \text{ s}^{-1}$
df/dy	β_0	$2.0 \times 10^{-11} \text{ m}^{-1} \text{ s}^{-1}$
Gravitational Acceleration	g	9.8 m s^{-2}
Reduced Gravity	g'	$2.0 \times 10^{-2} \text{ m s}^{-2}$
Horizontal Eddy Viscosity Coef.	A_h	$5.0 \times 10^2 \text{ m}^2 \text{ s}^{-1}$
Time Step	Δt	3600 s
Grid Increment in x-direction	Δx	10 km
Grid Increment in y-direction	Δy	10 km
Jet Maximum, Upper Layer	V_{1j}	0.4 m s^{-1} (southward)
Jet Maximum, Lower Layer	V_{2j}	0.01 m s^{-1} (southward)
Eddy Maximum, Upper Layer	V_{1e}	0.4 m s^{-1} (anticyclonic)
Eddy Maximum, Lower Layer	V_{1e}	0.4 m s^{-1} (anticyclonic)
Jet Position Offshore	L_j	50 km (from east wall)
Eddy Position Offshore	L_e	200 km (from east wall)
Basin Rotation Angle	γ	90° (from east)

Figures 2.5 and 2.6 show the reference state model output fields for height anomalies and upper layer velocities respectively. For this and all subsequent model

output field plots, surface height anomaly is contoured in cm, interface height anomaly is contoured in m and the velocities are contoured in cm/s. Based on the directional characteristics and the magnitudes of the flows, it is apparent that some phenomenon very similar to filament formation is occurring. Of particular note is the velocity structure of the offshore flow versus the inshore flow. The offshore flow has strong unidirectional flow while the inshore flow is slower and has more directional variability. The maximum offshore velocity by day 30 is about 50 cm/s and the inshore flow maximum about 40 cm/s. This type of structure and magnitude of flow correlates well with observed data in filament studies (Flament *et al.*, 1985; Kosro, 1987).

There are also two important signatures of baroclinic instability in the output fields: (1) wave growth in the initially nearly quiescent lower layer is indicative of vertical energy transfer from the upper to lower layer, and (2) there is a 180° phase shift between the waves in the upper layer and the waves in the lower layer.

2. Variation of Parameters

Structures shown in Figure 2.5 are consistent with observations of the form and magnitude of filaments. In order to isolate potential causes for filaments, the assumptions that the wave structures in Figure 2.5 represent filament formation and growth are made. Since the reference state is as complex as possible, the variations of the numerical simulations are largely one of simplification in specific areas of the model to see whether filaments are altered or made non-existent.

All of the numerical simulations are for 30 days and certain parameters from Table 1 are never varied. Table 2 provides a list of those parameters which are varied in the different experiments and what their reference state value is.

a. Experiment No. 1 (H_1 Increased to 250 m)

Upper layer thickness was increased to 250 m to determine the model sensitivity to the vertical structure. Figure 2.7 shows the model output fields for surface and interface height anomalies. From the fields, it is apparent that the wave structures are significantly different than those in the reference state. They are weaker and seem to stop growing halfway through the sequence. This points to the importance of the vertical structure to the wave development process.

b. Experiment No. 2 (Eddy Removed)

The eddy was removed in this experiment to determine whether it was responsible for the wave structures by its interaction with the coastal jet. Figure 2.8 shows the output fields for surface and interface height anomalies. The results are very

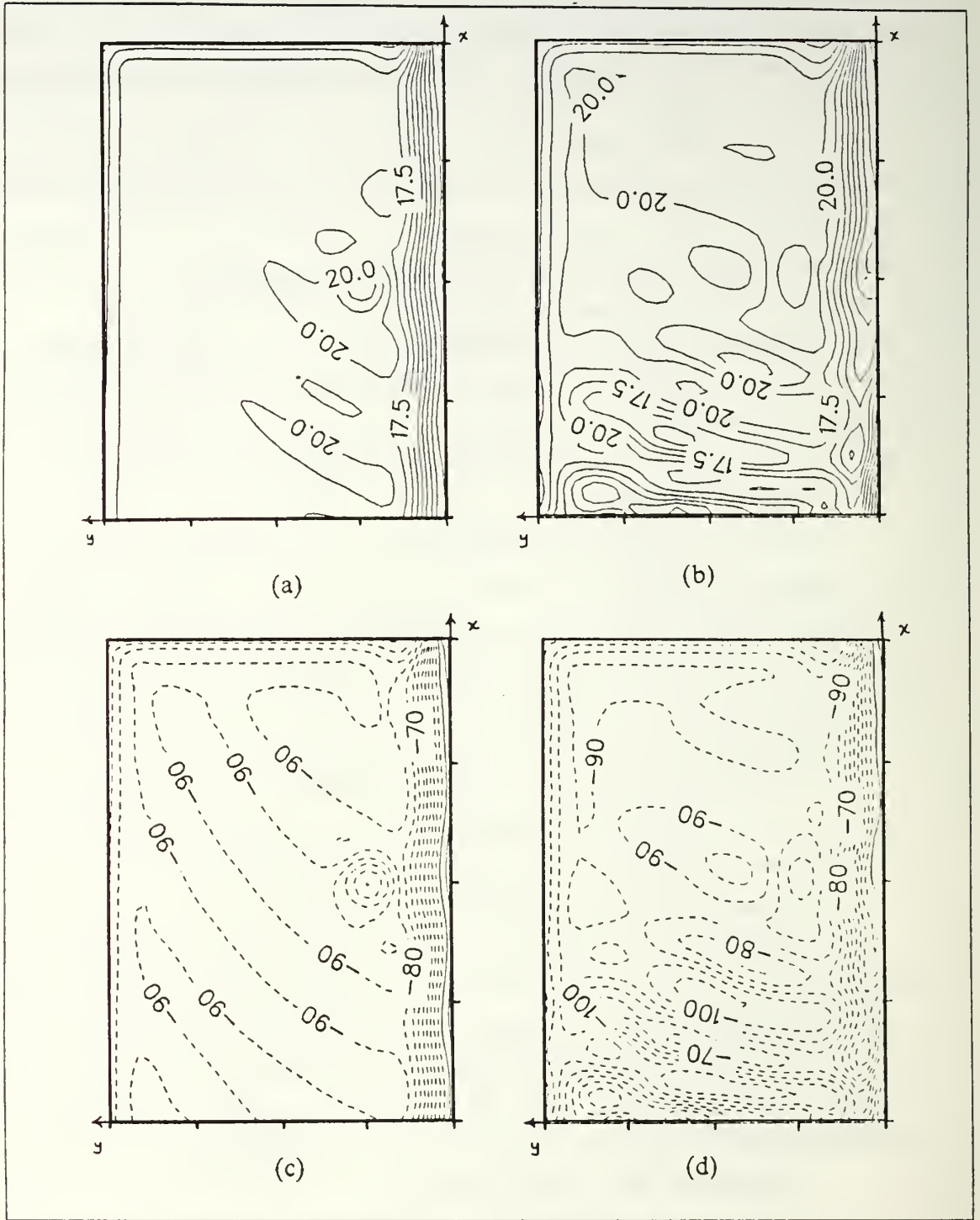


Figure 2.5 Model Output Fields of Height Anomalies for Reference State.

Height anomaly fields for (a) surface at day 15 (cm), (b) surface at day 30 (cm), (c) interface at day 15 (m), and (d) interface at day 30 (m).

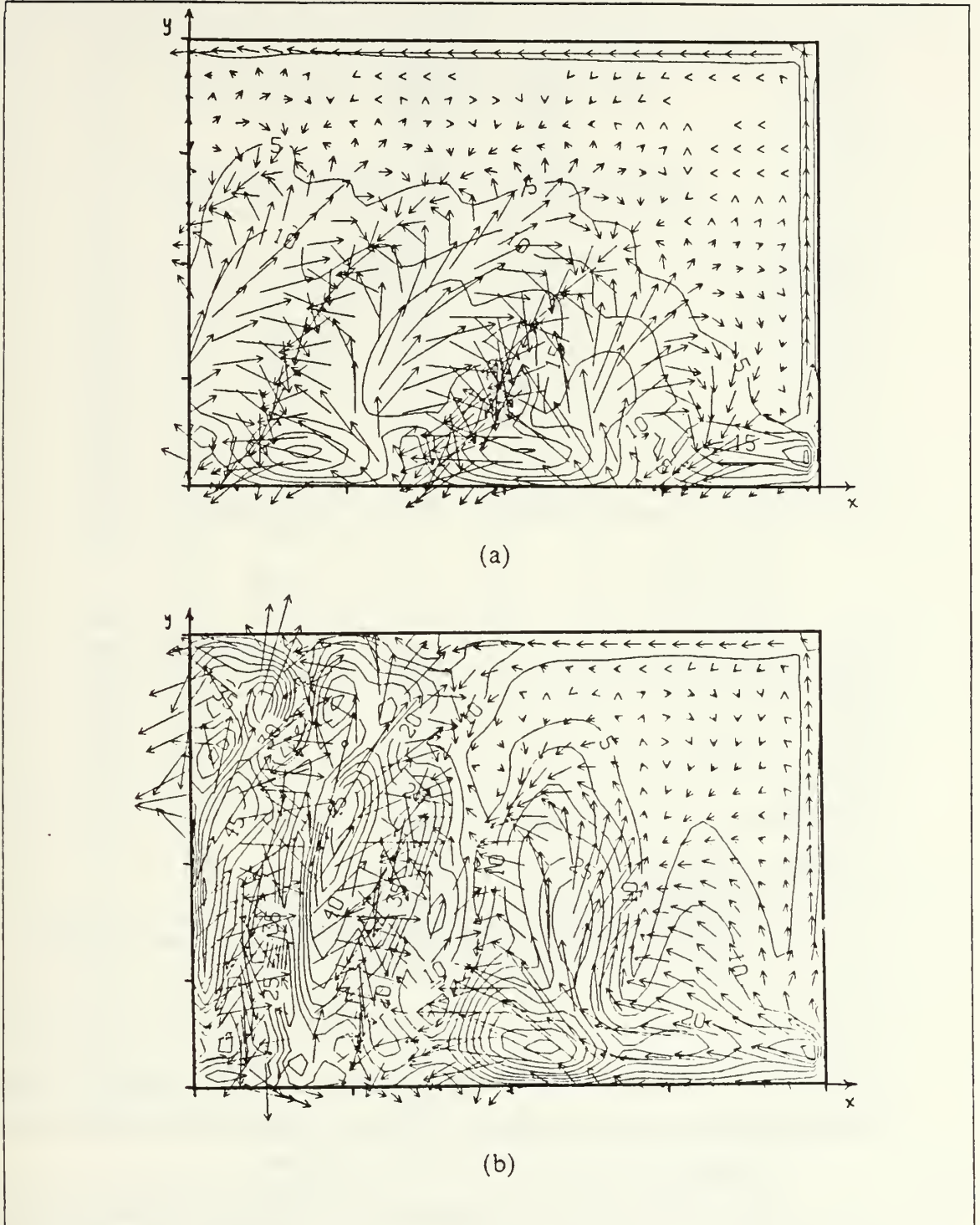


Figure 2.6 Model Output Fields of Upper Layer Velocity for Reference State.

Velocity fields (cm/s) for (a) upper layer at day 15 and (b) upper layer at day 30.

TABLE 2
VARIATION OF MODEL PARAMETERS

PARAMETER VALUES (Notation from Table 1)

Exp. #	H ₁	D(x,y)	V _{1j}	V _{2j}	V _{1e}	V _{2e}	L _j	L _e	γ
ref.	150	1	-.4	-.01	-.4	-.01	50	200	90
1.	250	1	-.4	-.01	-.4	-.01	50	200	90
2.	150	1	-.4	-.01	ne	ne	50	200	90
3.	150	1	-.4	-.01	-.4	-.01	150	300	90
4.	150	0	-.4	-.01	-.4	-.01	50	200	90
5.	150	1	-.4	-.05	-.4	-.05	50	200	90
6.	150	1	-.4	.01	-.4	.01	50	200	90
7.	150	1	-.4	-.01	-.4	-.01	50	200	0
8.	150	1	-.4	-.01	-.4	-.01	50	200	180
9.	150	0	-.4	-.01	ne	ne	50	200	90
10.	150	1	-.4	-.01	ne	ne	50	200	120
11.	150	1	-.2	-.01	-.2	-.01	50	200	90
12.	150	1	-.1	-.01	-.1	-.01	50	200	90

Notes: (1) Depths in m
 (2) Lengths in km
 (3) Velocities in m/s, + to north, - to south
 (4) Bottom depth: 1 topography, 0 flat bottom
 (5) Eddy rotation: CW for + vel., CCW for - vel.; ne = no eddy
 (6) Basin rotation angle (γ) in degrees from east

similar to the reference state. The wave structure is more uniform in this run, indicating that the eddy is not causative. However, it does affect the wave structure.

c. Experiment No. 3 (Jet Moved Farther Offshore)

The jet and the eddy were moved out farther away from the coast to see if wave structures were being generated as a result of boundary interactions with the eastern, no-slip boundary. Figure 2.9 shows the output fields for this run. In general, the results are very comparable to the reference state. It looks as though the full

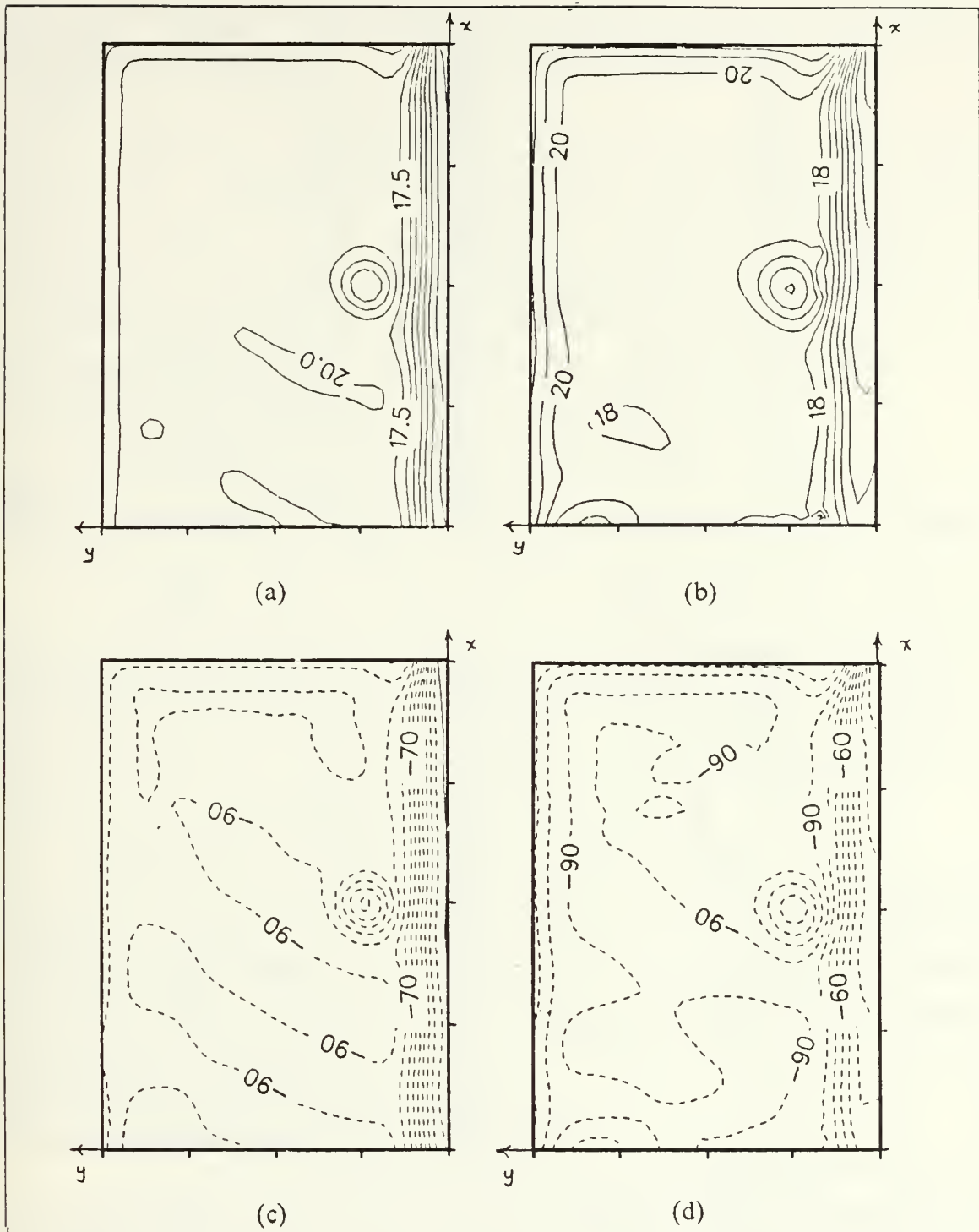


Figure 2.7 Experiment # 1 (H_1 Increased to 250 m)
Model Output Height Anomalies.

Height anomaly fields for (a) surface at day 15 (cm), (b) surface at day 30 (cm), (c) interface at day 15 (m), and (d) interface at day 30 (m).

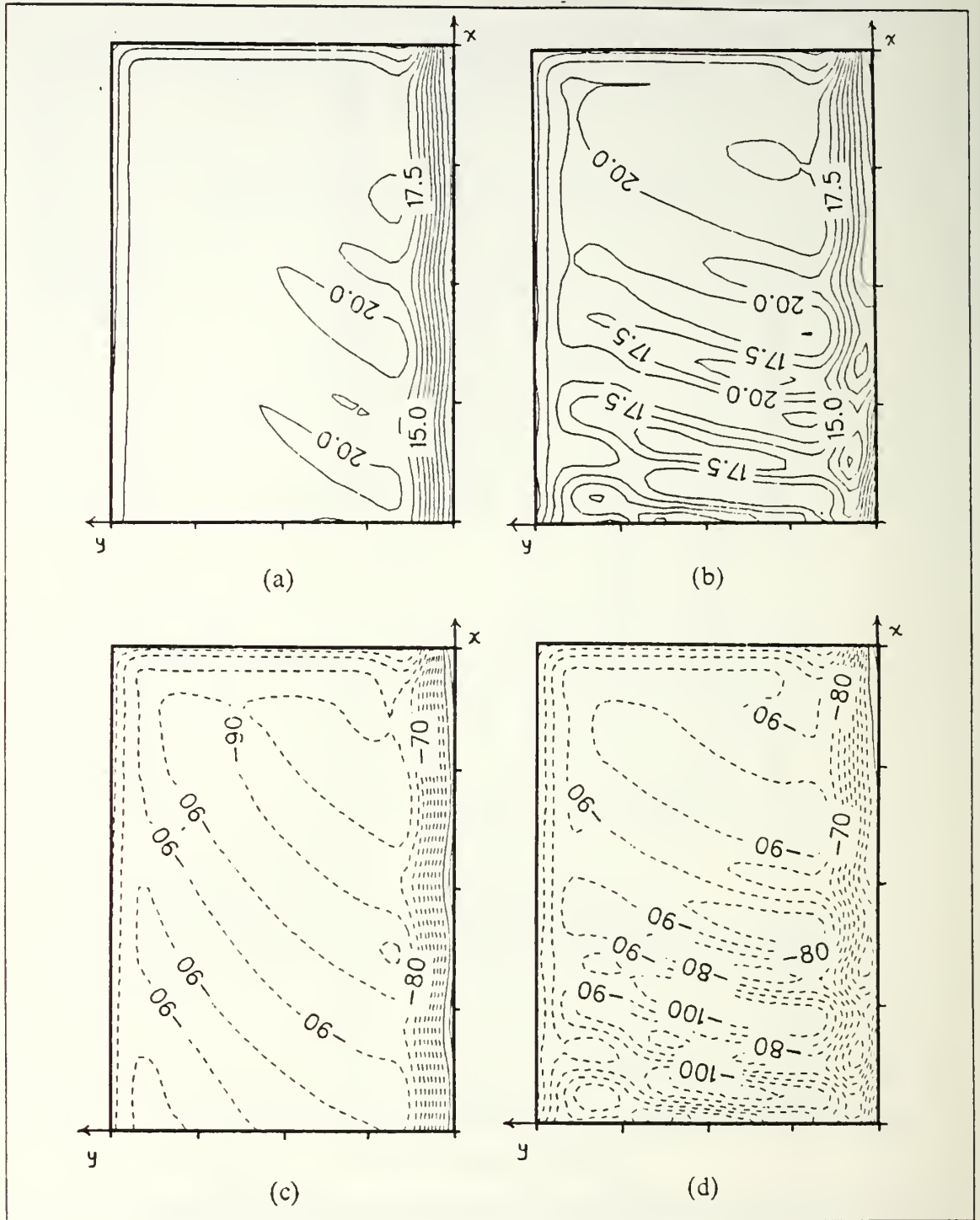


Figure 2.8 Experiment # 2 (Eddy Removed)
Model Output Height Anomalies.

Height anomaly fields for (a) surface at day 15 (cm), (b) surface at day 30 (cm), (c) interface at day 15 (m), and (d) interface at day 30 (m).

growth and extent of the waves to the west is now being hindered but their structure is consistent. Apparently, the boundaries can restrict but cannot generate the disturbances.

d. Experiment No. 4 (Topography Removed)

In this case, topography was removed and a flat bottom at 4500 m depth utilized. There is substantial circumstantial evidence linking filaments to coastal topographic features such as the Mendocino Escarpment. By removing the topography, it is hoped that it can be determined whether bottom variations are causing the filament formation. Figure 2.10 shows the output fields for this run. The fields are nearly identical with the reference run. Apparently, topography is not inducing the filament formation process for this weak lower layer flow.

e. Experiment No. 5 (Increased Lower Layer Velocity)

In this run the lower layer velocity was increased from 1 cm/s to 5 cm/s flowing southward, which is considered to be on the order of the maximum observed velocity in the deep water south of Cape Mendocino (Stabeno and Smith, 1987). This reduces the vertical shear but increases significantly the model coupling with the bottom. Although the previous run tended to discount the importance of the bottom, it is important to see what possible effects it might have in a worst case situation. Figure 2.11 shows the output fields over the domain. The results are nearly identical with the reference state with the amplitudes slightly smaller. This indicates that the model is relatively insensitive to southward lower layer velocity.

f. Experiment No. 6 (Lower Layer Flow Direction Reversed)

In this experiment, the lower layer flow was reversed so that it was flowing opposite the upper layer flow. This effectively increases the vertical velocity shear and examines a possible configuration of the CCS where there is a deep, weak northward flow. Figure 2.12 shows the output fields for this run. The wave structure is similar to, yet noticeably stronger than, the reference. This would indicate the wave growth to be very sensitive to the vertical velocity shear.

g. Experiment No. 7 (Zonal Flow Westward)

In order to perform a sort of check on the model dynamics, the basin was not rotated into its CCS position. Since most instability studies are concerned with zonal rather than meridional flows, the analytic analysis of this type of problem is common and the expected dynamics are supported by observational data. With $\gamma = 0$, the jet is westward and the eddy rotates as before, anticyclonically. Figure 2.13 shows

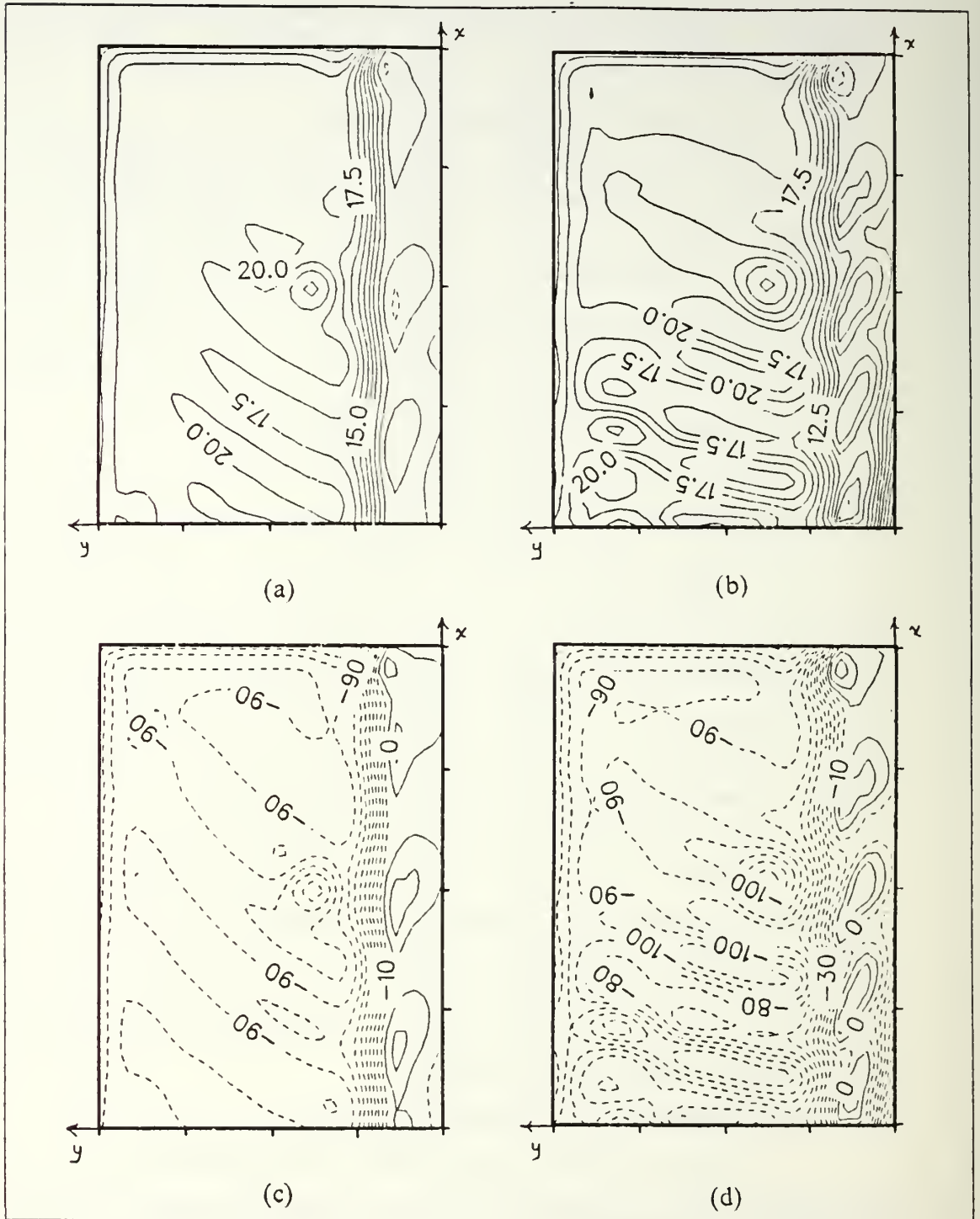


Figure 2.9 Experiment # 3 (Jet Moved Farther Offshore)
 Model Output Height Anomalies.

Height anomaly fields for (a) surface at day 15 (cm), (b) surface at day 30 (cm), (c) interface at day 15 (m), and (d) interface at day 30 (m).

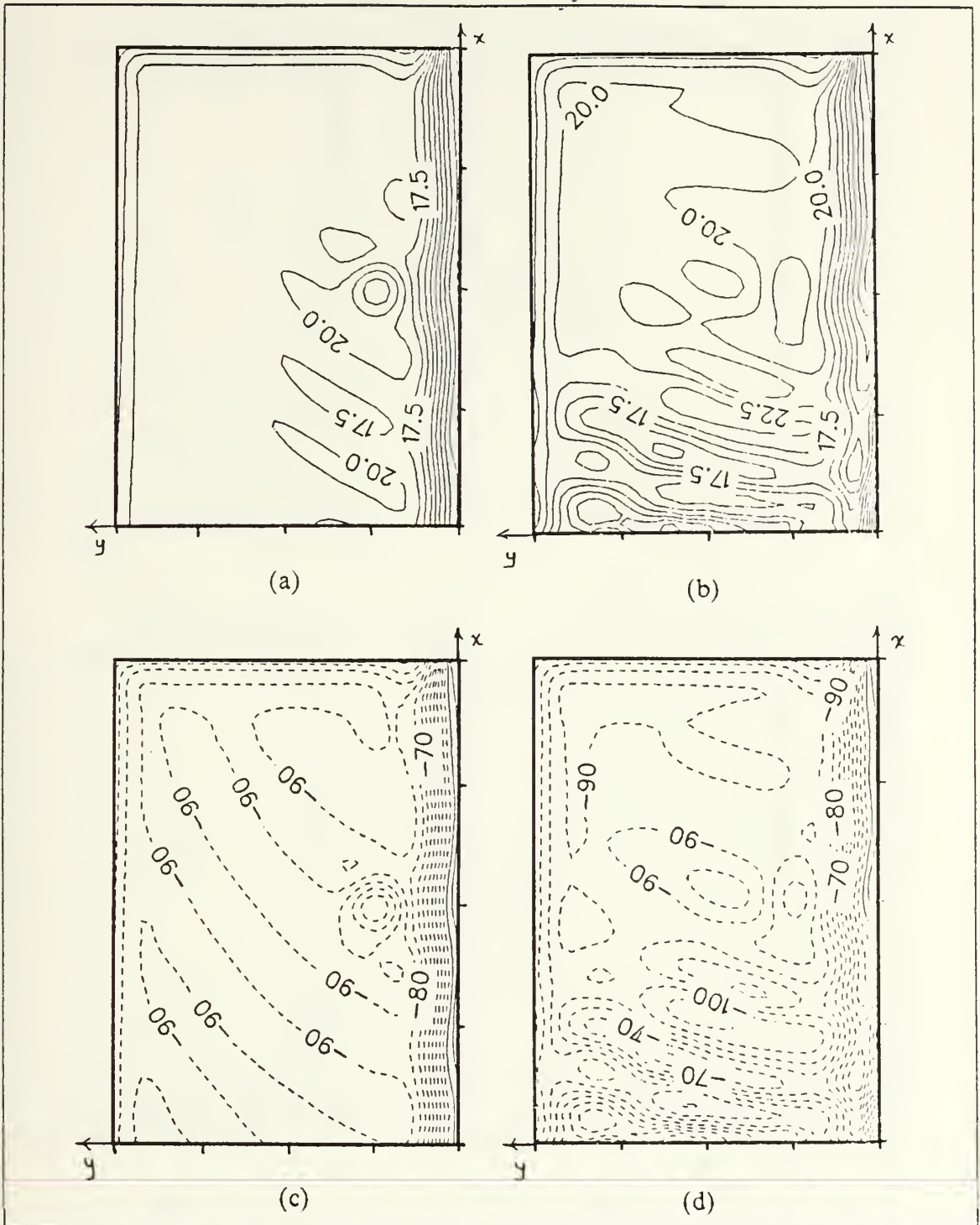


Figure 2.10 Experiment # 4 (Topography Removed)
Model Output Height Anomalies.

Height anomaly fields for (a) surface at day 15 (cm), (b) surface at day 30 (cm), (c) interface at day 15 (m), and (d) interface at day 30 (m).

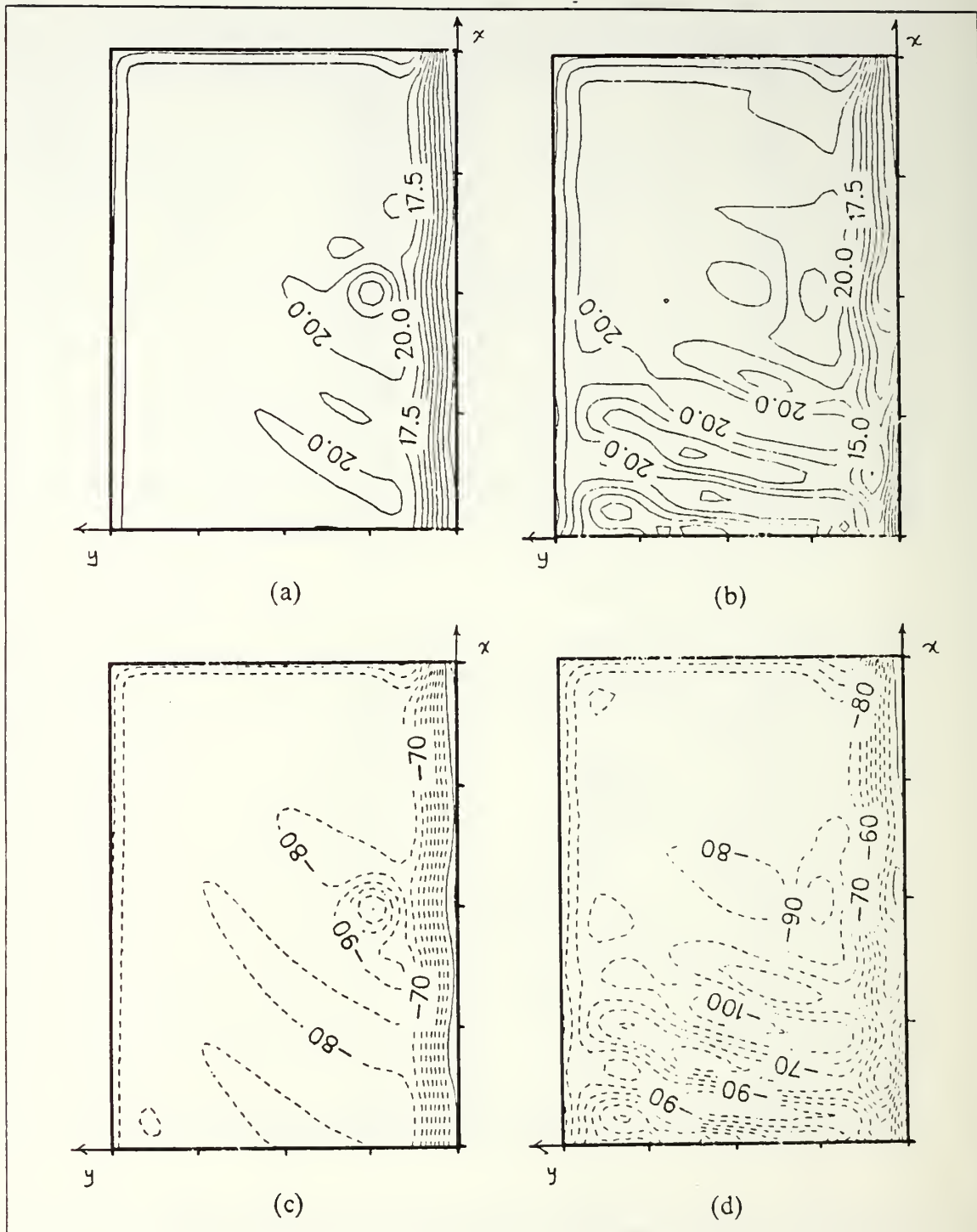


Figure 2.11 Experiment # 5 (Increased Lower Layer Velocity)
Model Output Height Anomalies.

Height anomaly fields for (a) surface at day 15 (cm), (b) surface at day 30 (cm), (c) interface at day 15 (m), and (d) interface at day 30 (m).

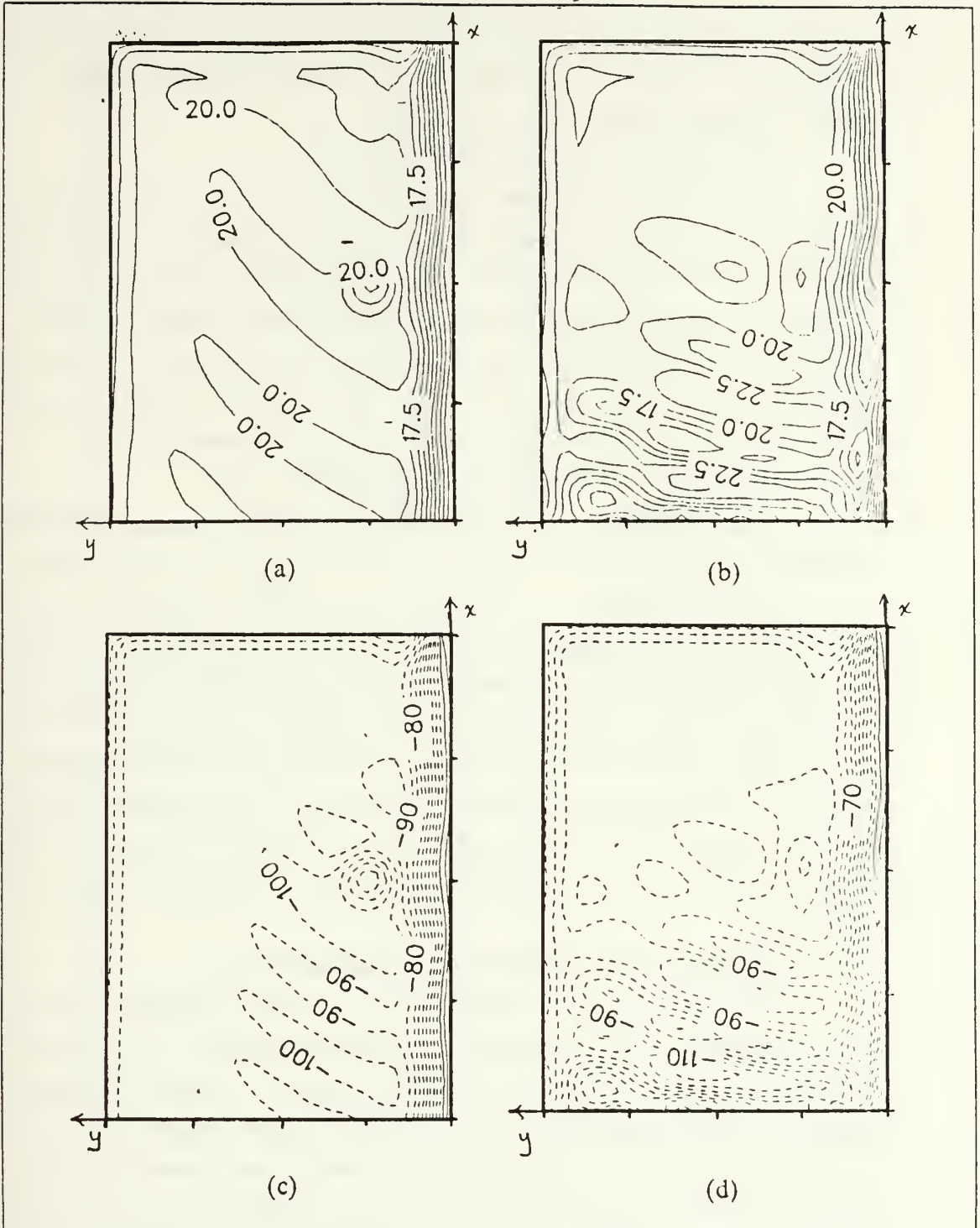


Figure 2.12 Experiment # 6 (Lower Layer Flow Direction Reversed)
Model Output Height Anomalies.

Height anomaly fields for (a) surface at day 15 (cm), (b) surface at day 30 (cm), (c) interface at day 15 (m), and (d) interface at day 30 (m).

the output from this simulation. It is readily apparent that there are some type of instabilities in the flow but they are substantially reduced from the cases where there was meridional flow. This makes sense from a linear instability standpoint and will be clarified in the next chapter.

h. Experiment No. 8 (Zonal Flow Eastward)

As with the previous experiment, the basin was not rotated into its standard CCS orientation. To examine the model response for a jet flowing zonally eastward, the basin was rotated 180° . As mentioned before, the dynamics of this type of configuration are well known and should help verify the model responses. Figure 2.14 shows the output fields for this run. Of note is the fact that the flow is almost completely stable throughout the model run. Again, this makes sense from a dynamical standpoint and will also be addressed in the following chapter.

i. Experiment No. 9 (Eddy and Topography Removed)

In experiment # 2 the eddy was removed and in experiment # 4 topography was eliminated. This does not totally resolve their involvement with the wave structure development. A requirement for baroclinic instability is a perturbation of the mean flow. It is conceivable that the eddy and the topography could be causing the jet to be deflected so as to undergo perturbation growth by instability theory. To see whether this is true, both the eddy and topography were removed for this run. As can be seen in Figure 2.15, the removal of both the eddy and topography did not hinder at all the development of the wave structures. There are some slight differences from the reference state run, but they are so small that it would be difficult to speculate as to their exact connection with the altered conditions of this run vice the reference one.

j. Experiment No. 10 (Northwest to Southeast Flow)

As can be seen in Figure 2.1, the coastline south of Cape Mendocino changes orientation from north-south to northwest-southeast. To examine the effects of this orientation on the flow the basin was rotated 120° as shown in the figure by the dotted box. This new configuration is important to the degree of applicability the model results will have to the CCS. It is obvious that the coastal jet cannot continue straight south after Cape Mendocino and if wave structures are not observed with the modeled jet going southeast it is doubtful whether the meridional flow results are true representations of the dynamics of the CCS. Figure 2.16 shows the model response to the basin rotation of 120° . The eddy was removed from this run so the wave structure

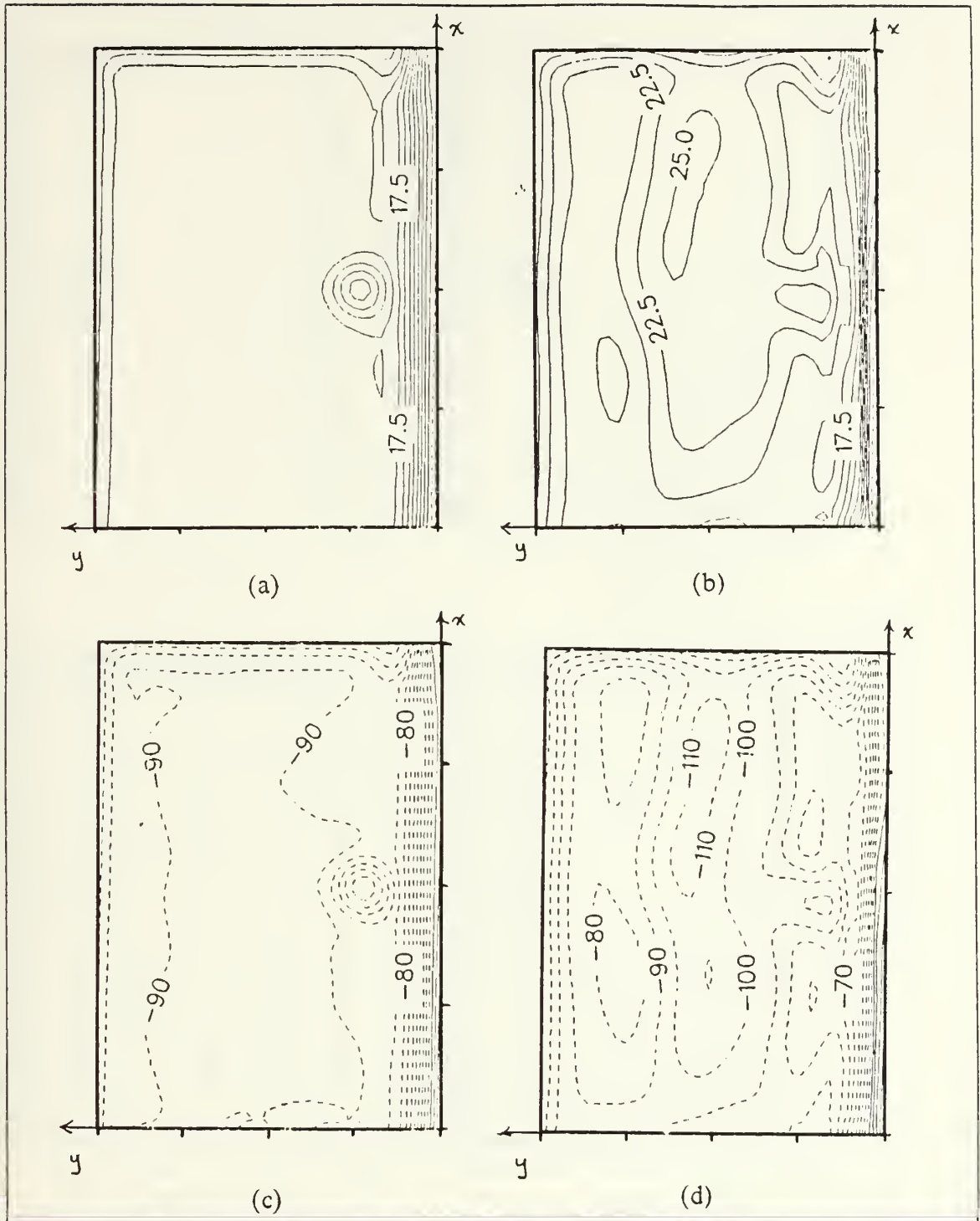


Figure 2.13 Experiment # 7 (Zonal Flow Westward)
Model Output Height Anomalies.

Height anomaly fields for (a) surface at day 15 (cm), (b) surface at day 30 (cm), (c) interface at day 15 (m), and (d) interface at day 30 (m).

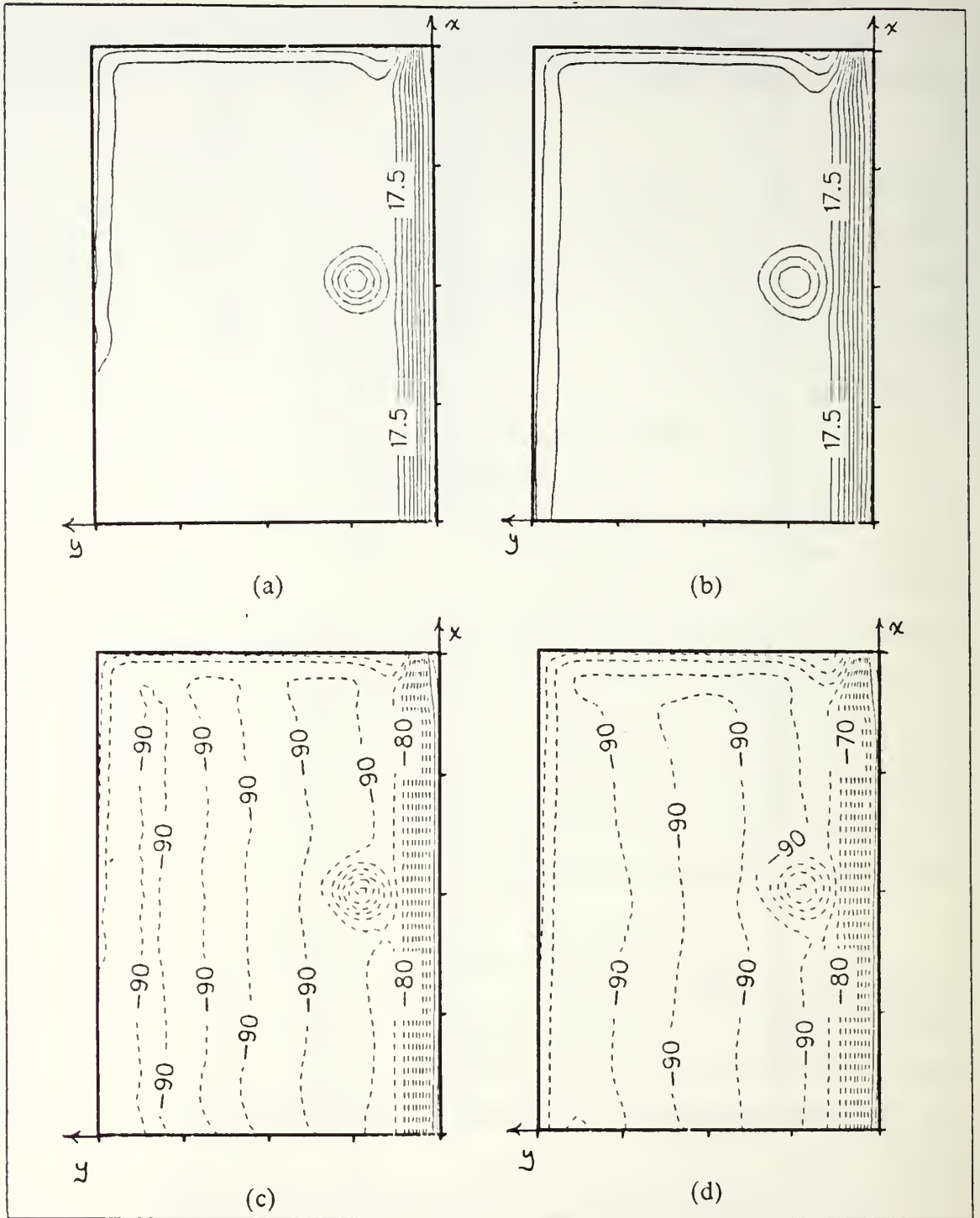


Figure 2.14 Experiment # 8 (Zonal Flow Eastward)
Model Output Height Anomalies.

Height anomaly fields for (a) surface at day 15 (cm), (b) surface at day 30 (cm), (c) interface at day 15 (m), and (d) interface at day 30 (m).

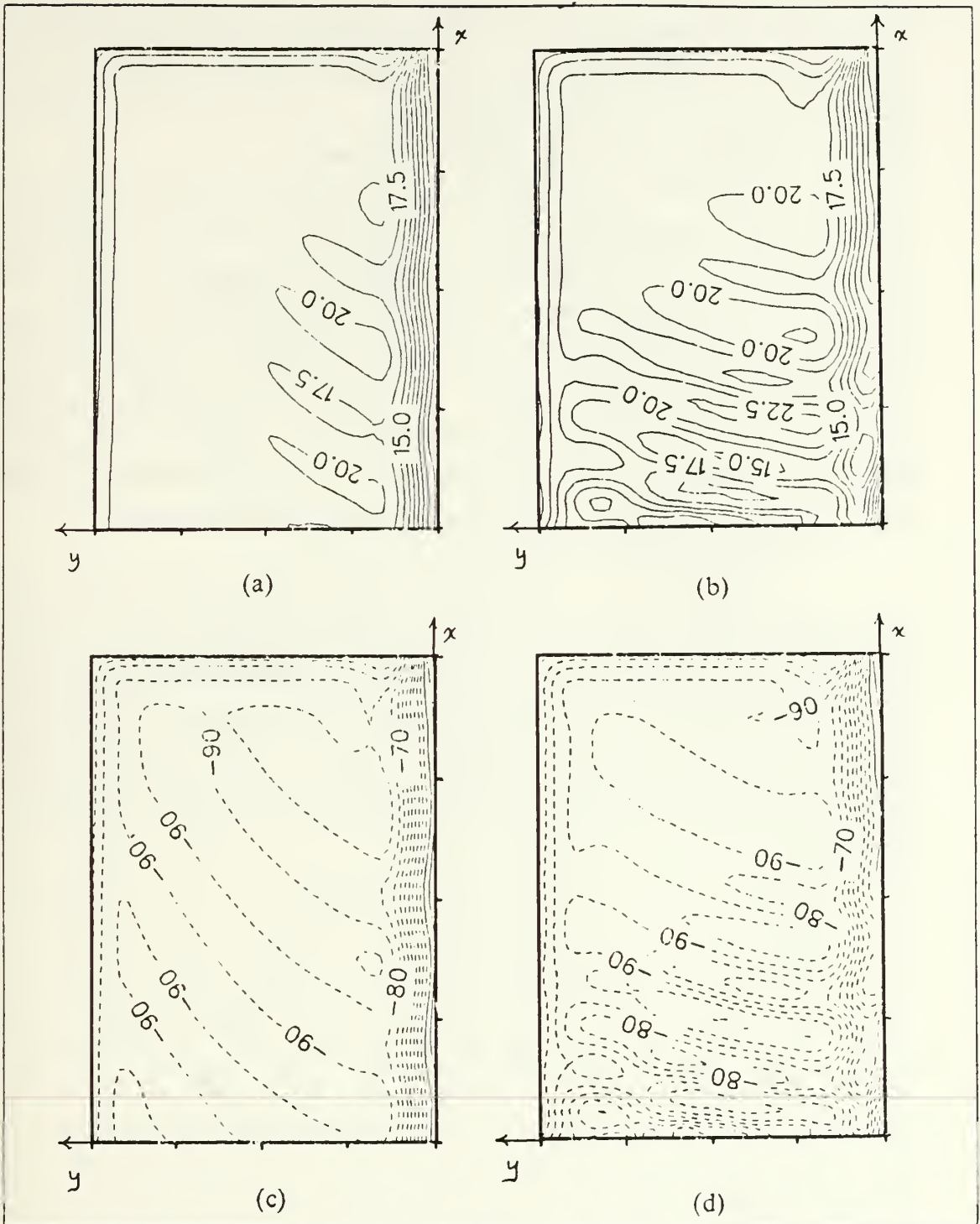


Figure 2.15 Experiment # 9 (Eddy and Topography Removed)
Model Output Height Anomalies.

Height anomaly fields for (a) surface at day 15 (cm), (b) surface at day 30 (cm), (c) interface at day 15 (m), and (d) interface at day 30 (m).

changes could be better seen. There are substantial differences from the reference but they are clearly in terms of the wave structure direction and wavelength rather than representing a totally different type of phenomenon. In the next chapter, the reasons for these structural differences will be examined.

k. Experiment No. 11 (V_{1j} Reduced to 0.2 m/s)

Up until now all of the model runs have used an upper layer velocity of 0.4 m/s. This may be representative of the CCS at certain times but by no means is the CCS consistent. As with the previous experiment, applicability to the real world demands that the model parameters be as realistic as possible in both value and range. The velocity is reduced to 0.2 m/s thus effectively halving the vertical shear. Figure 2.17 shows the results of this alteration. The wave structures are definitely present in a form similar to the reference although their strength is considerably less. This makes sense from an instability standpoint as the shear and thus available potential energy of the system has been reduced. This will be discussed in the next chapter.

l. Experiment No. 12 (V_{1j} Reduced to 0.1 m/s)

As a follow on to the previous experiment, the upper layer velocity is reduced again by fifty percent. The results are indicated in Figure 2.18. There is some very slight wave development but it is considerably less than either the previous case or the reference state. This would intuitively mean that the reduction of the upper layer velocity is causing the system to approach a point of stability. The fact that the system is becoming stable with a shear still present will be covered also in the next chapter.

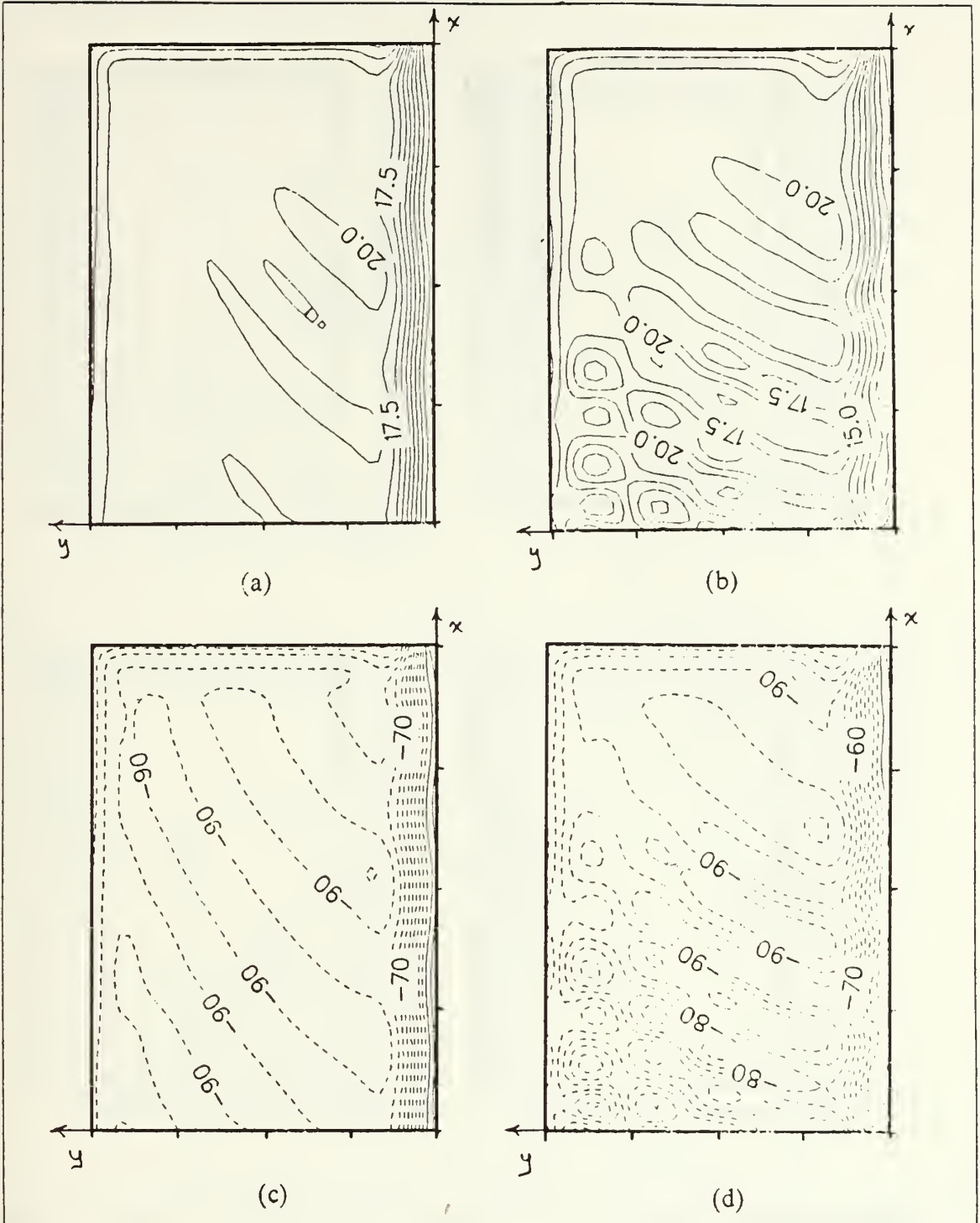


Figure 2.16 Experiment #10 (Northwest to Southeast Flow)
Model Output Height Anomalies.

Height anomaly fields for (a) surface at day 15 (cm), (b) surface at day 30 (cm), (c) interface at day 15 (m), and (d) interface at day 30 (m).

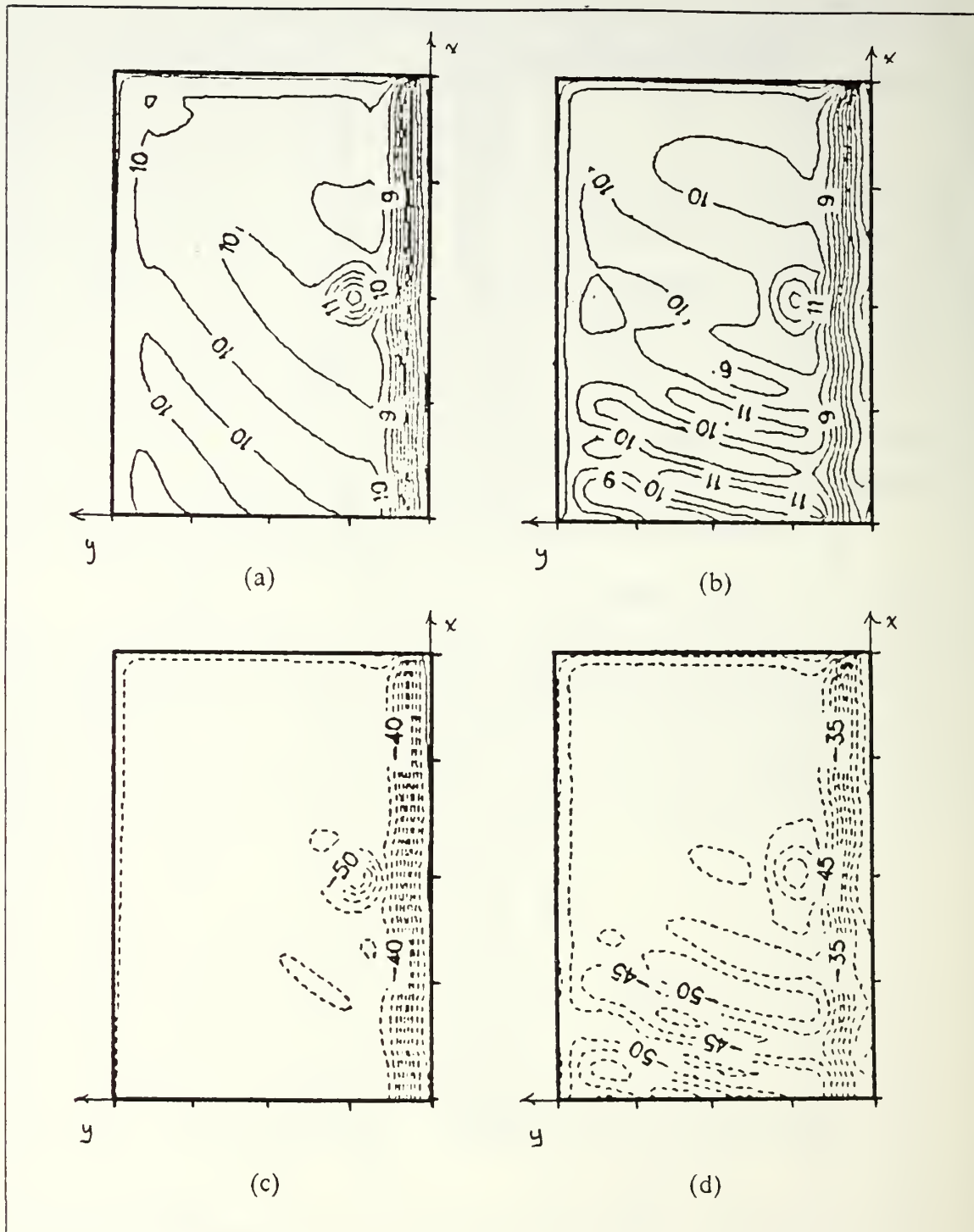


Figure 2.17 Experiment #11 (V_{1j} Reduced to 0.2 m/s)
Model Output Height Anomalies.

Height anomaly fields for (a) surface at day 15 (cm), (b) surface at day 30 (cm), (c) interface at day 15 (m), and (d) interface at day 30 (m).

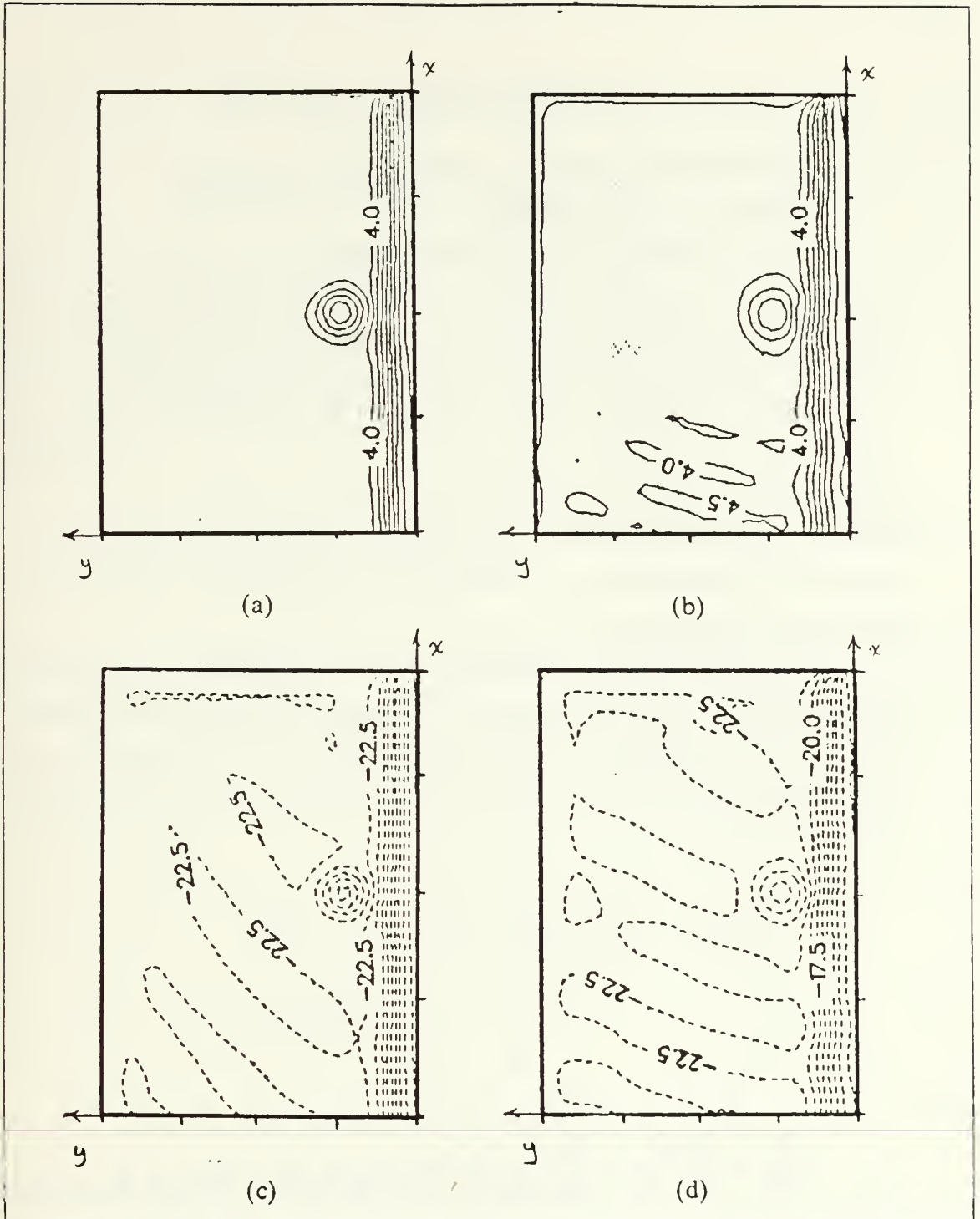


Figure 2.18 Experiment #12 (V_{1j} Reduced to 0.1 m/s)
Model Output Height Anomalies.

Height anomaly fields for (a) surface at day 15 (cm), (b) surface at day 30 (cm), (c) interface at day 15 (m), and (d) interface at day 30 (m).

III. BAROCLINIC ANALYSIS

A. SETTING UP THE LINEAR INSTABILITY PROBLEM

1. Instability of a Non-Zonal Flow

Most examinations of baroclinic instability start with the assumption of a zonal flow. This assumption cannot be made when dealing with the CCS where the basic state is definitely non-zonal and in some regions completely meridional. To develop an analytic model for the CCS, the quasigeostrophic equations of motion will be employed. This represents a divergence from the model dynamics which are operating under the primitive equations. To evaluate whether the quasigeostrophic equations are reasonable approximations, the Rossby number, Ro , can be calculated. Using $U = 0.4$ m/s, $f = 0.94 \times 10^{-4}$ s⁻¹ and $L = R_d = 18.4$ km yields $Ro = 0.23$. This indicates that nonlinearities are appreciable but the quasigeostrophic equations should be within the required accuracy.

A non-zonal flow automatically implies the existence of an external forcing field (Pedlosky, 1979). In this case, it is assumed that the external forcing involved with the CCS is wind stress curl. For a two layer system without bottom friction the governing quasigeostrophic potential vorticity equations in non-dimensional form from Pedlosky (1979) are:

$$\left[\frac{\partial}{\partial t} + \frac{\partial \psi_1}{\partial x} \frac{\partial}{\partial y} - \frac{\partial \psi_1}{\partial y} \frac{\partial}{\partial x} \right] [\nabla^2 \psi_1 - F_1(\psi_1 - \psi_2) + \beta y] = \left[\frac{\tau_0}{\rho_0 f_0 U D_1} \right] k \cdot \text{curl } \tau \quad (3.1)$$

$$\left[\frac{\partial}{\partial t} + \frac{\partial \psi_2}{\partial x} \frac{\partial}{\partial y} - \frac{\partial \psi_2}{\partial y} \frac{\partial}{\partial x} \right] [\nabla^2 \psi_2 - F_2(\psi_2 - \psi_1) + \beta y] = 0 \quad (3.2)$$

Notation is defined in the Appendix.

Following the derivation by Pedlosky (1979) for the phase speed of a baroclinic wave in a non-zonal flow, consider the following basic state:

$$\psi_1 = \Psi_1 = v_1 x - u_1 y \quad (3.3)$$

$$\Psi_2 = \Psi_1 = 0 \quad (3.4)$$

The parameters u_1 and v_1 are constant velocities in the upper layer in the x and y direction respectively. Note that the basic state is characterized by a uniform flow which does not vary in the cross stream direction. This will inherently eliminate barotropic instability from the analytic development but due to the length scales of the instabilities observed in the model runs ($L \gg R_d$), barotropic instability is not likely to be a dominant force (Kamenkovich *et al.*, 1986). There are no boundary constraints on the basic flow eliminating shear induced vorticity which is present in the numerical model. Again, it is felt that this will primarily affect barotropic instability modes. The wall effects on baroclinic instability are considered negligible. As Mysak *et al.* (1981) pointed out,

. . . inclusion of vertical side walls at the edges of a coastal current flowing along a continental slope does not significantly affect the growth rate, frequency or wavelength of the maximum unstable wave

The real motivation for making these assumptions is that the analytic modeling of a non-uniform, non-zonal flow with boundary effects would be far beyond the scope of this presentation and would probably not yield significantly different results. Model runs with small flows in the lower layer in both a north and south direction were so similar that the assumption of no flow in the lower layer should be consistent with the numerical model.

To examine the stability of the basic state, consider perturbations of the following form:

$$\Psi_1 = \Psi_1 + \phi_1(x,y,t) \quad (3.5)$$

$$\Psi_2 = \Psi_2 + \phi_2(x,y,t) \quad (3.6)$$

Substitution into 3.1 and 3.2 and linearization yields

$$\begin{aligned} \left[\frac{\partial}{\partial t} + u_1 \frac{\partial}{\partial x} + v_1 \frac{\partial}{\partial y} \right] [\nabla^2 \phi_1 - E_1 (\phi_1 - \phi_2)] \\ + (\beta + E_1 u_1) \frac{\partial \phi_1}{\partial x} + E_1 v_1 \frac{\partial \phi_1}{\partial y} = 0 \end{aligned} \quad (3.7)$$

$$\left[\frac{\partial}{\partial t} \right] [\nabla^2 \varphi_2 - E_2 (\varphi_2 - \varphi_1)] + (\beta - E_2 u_1) \frac{\partial \varphi_2}{\partial x} - E_2 v_1 \frac{\partial \varphi_2}{\partial y} = 0 \quad (3.8)$$

Note that the wind stress curl forcing does not appear in the perturbation equations. As Pedlosky (1979) describes it,

. . . the stability of basic flows which are not solutions of the *unforced* equations of motion may be consistently considered in the context of the *unforced* perturbation equations, without the need to consider explicitly the forces required to produce a basic state.

This provides the basis for not specifying the form of the wind stress curl in 3.1.

Using the normal mode approach, plane wave solutions of the following form are assumed:

$$\psi_n = A_n \exp i(kx + \ell y - \sigma t) \quad n = 1, 2 \quad (3.9)$$

Substitution into 3.7 and 3.8 leads to

$$A_1 [(\sigma - u_1 k - v_1 \ell) (K^2 + E_1) + \beta k + E_1 (u_1 k + v_1 \ell)] - A_2 E_1 (\sigma - u_1 k - v_1 \ell) = 0 \quad (3.10)$$

$$A_2 [\sigma (K^2 + E_2) + \beta k - E_2 (u_1 k + v_1 \ell)] - A_1 E_2 \sigma = 0 \quad (3.11)$$

$$\text{where } K^2 = k^2 + \ell^2$$

A coordinate system is now defined as shown in Figure 3.1. The angle the perturbation wave vector makes with the x-axis is θ while α represents the angle the shear flow makes with the x-axis.

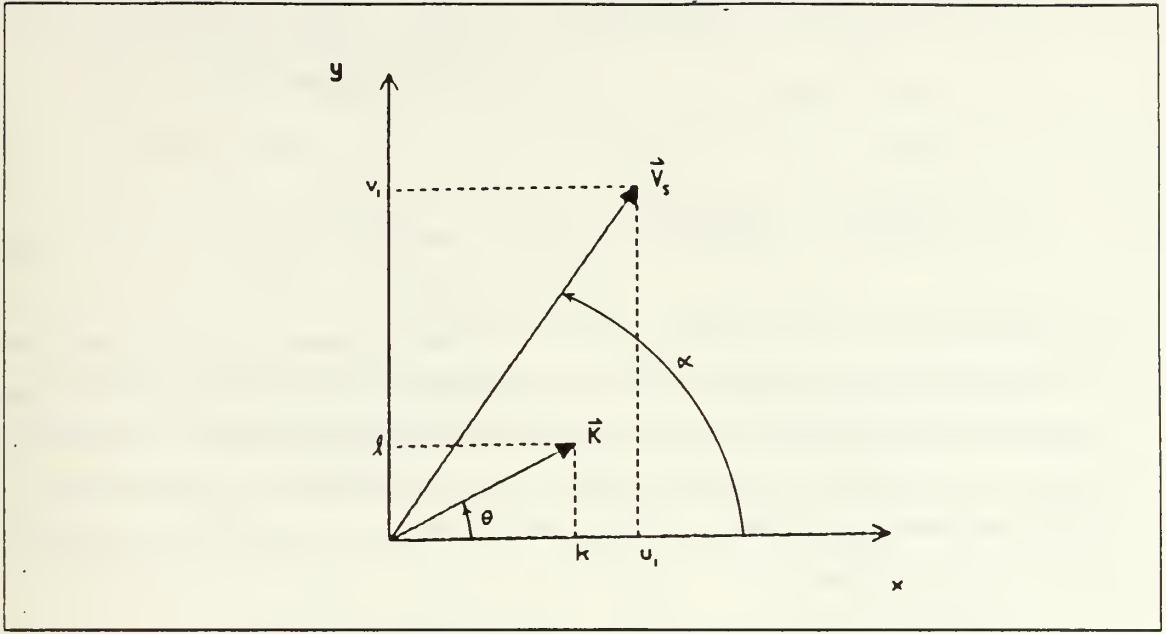


Figure 3.1 Coordinate System Orientation.

Based on the flow directions of the CCS within the numerical model domain noted in section II.A, α can take on only one of two values, 270° or 300° . The coordinate system allows the following transformations and the introduction of the shear velocity, V_s :

$$\beta k / \mathbf{K} = \beta \cos \theta \quad (3.12)$$

$$(u_1 k + v_1 l) / \mathbf{K} = V_s \cos(\alpha - \theta) \quad (3.13)$$

$$\text{Where } V_s = (u_1^2 + v_1^2)^{1/2}$$

The perturbation wave phase speed c is allowed to take on complex values,

$$c = \sigma / \mathbf{K} = c_r \pm ic_i \quad (3.14)$$

After dividing 3.10 and 3.11 by \mathbf{K} , use of 3.12, 3.13 and 3.14 results in,

$$A_1[(c - V_S \cos(\alpha - \theta))(K^2 + F_1) + \beta \cos \theta + F_1 V_S \cos(\alpha - \theta)] \quad (3.15)$$

$$- A_2 F_1 (c - V_S \cos(\alpha - \theta)) = 0$$

$$A_2[c(K^2 + F_2) + \beta \cos \theta - F_2 V_S \cos(\alpha - \theta)] - A_1 F_2 c = 0 \quad (3.16)$$

Nontrivial solutions for A_1 and A_2 exist only if the determinant of their coefficients in 3.15 and 3.16 is equal to zero. Since the basic intent of this analytic development is specifically to support analysis of the model output and the CCS it is more practical at this point to switch to dimensional form. Using the notation of Kamenkovich *et al.* (1986), the zero determinant condition leads to the phase speed of the perturbation wave (Equation 3.17).

$$c = \frac{V_S K^2 (K^2 + 2\Lambda_2) \cos(\alpha - \theta) - \beta (2K^2 + \Lambda_1 + \Lambda_2) \cos \theta}{2K^2 (K^2 + \Lambda_1 + \Lambda_2)}$$

$$\pm \frac{\{(\Lambda_1 + \Lambda_2)^2 \beta^2 \cos^2 \theta + 2\beta V_S K^4 (\Lambda_1 - \Lambda_2) \cos \theta \cos(\alpha - \theta) - K^4 V_S^2 (4\Lambda_1 \Lambda_2 - K^4) \cos^2(\alpha - \theta)\}^{1/2}}{2K^2 (K^2 + \Lambda_1 + \Lambda_2)} \quad (3.17)$$

Where $\Lambda_1 = F_1/L^2$, $\Lambda_2 = F_2/L^2$, $\beta = \beta_0$ and all velocities from before multiplied by scaling velocity U .

2. Critical Velocity and Growth Rate

When the radicand in 3.17 is equal to zero, the wave is at the transition point between stability and instability. At this point, V_S can be solved for. This results in an expression for the critical shear velocity for instability, V_{sc} .

$$V_{sc} = \frac{\beta K^2 (\Lambda_1 - \Lambda_2) \cos \theta \pm 2\beta (\Lambda_1 \Lambda_2)^{1/2} [(\Lambda_1 + \Lambda_2)^2 - K^4]^{1/2} \cos \theta}{K^2 (4\Lambda_1 \Lambda_2 - K^4) \cos(\alpha - \theta)} \quad (3.18)$$

Utilizing the two basic state flow directions to match the CCS ($\alpha = 270^\circ$, 300°) and using model values of $\Lambda_1 = 2.94 \times 10^{-9} \text{ m}^{-2}$, $\Lambda_2 = 1.02 \times 10^{-10} \text{ m}^{-2}$ and $\beta = 2.0 \times 10^{-11} \text{ m}^{-1} \text{ s}^{-1}$ leaves V_{sc} a function of only K and θ . Figures 3.2 and 3.3 show the marginal stability curves for α of 270° and 300° respectively for various perturbation wave directions, θ . Note that curves are not shown for cases where the wave direction is perpendicular to the flow direction since by 3.18 this results in infinite shear velocities and no instability is possible. The form of the marginal stability is determined by the quadrant that θ is in. The unstable region is shaded and represents the area where the shear velocity is greater than required for instability. The excess shear then becomes the energy source to provide a positive growth rate in those regions. The full implications of a meridional flow and a meridional wave direction are indicated by Figures 3.2b and 3.2e.. The required shear flow goes to zero and thus any non-zero shear will result in instability as long as the wavenumber is to the left of the vertical asymptote corresponding to the condition,

$$K < (4\Lambda_1\Lambda_2)^{1/4} \quad (3.19)$$

which comes directly from Equation 3.18.

With the shear conditions for instability defined, the next step is to find the magnitude of the growth rate in the unstable regions. Growth rate values will provide the necessary information to determine the characteristics of the fastest growing wave. For an unstable wave to grow, the radicand of 3.17 must be negative and the growth rate, Kc_i becomes,

$$Kc_i = \frac{[K^4 V_s^2 (4\Lambda_1\Lambda_2 - K^4) \cos^2(\alpha - \theta) - 2\beta V_s K^4 (\Lambda_1 - \Lambda_2) \cos\theta \cos(\alpha - \theta) - (\Lambda_1 + \Lambda_2)^2 \beta^2 \cos^2\theta]^{1/2}}{2K(K^2 + \Lambda_1 + \Lambda_2)} \quad (3.20)$$

As before, model values for Λ_1 , Λ_2 and β along with flow angle α reduces the growth rate dependence to just V_s , θ and K . Figures 3.4 and 3.5 show the growth rates for $\alpha = 270^\circ$ and 300° respectively for velocity shears of 0.4, 0.3, 0.2 and 0.1 m/s. As expected, the growth rate magnitude is a strong function of the shear velocity since that provides the energy input into the growing wave. The maximum growth rate,

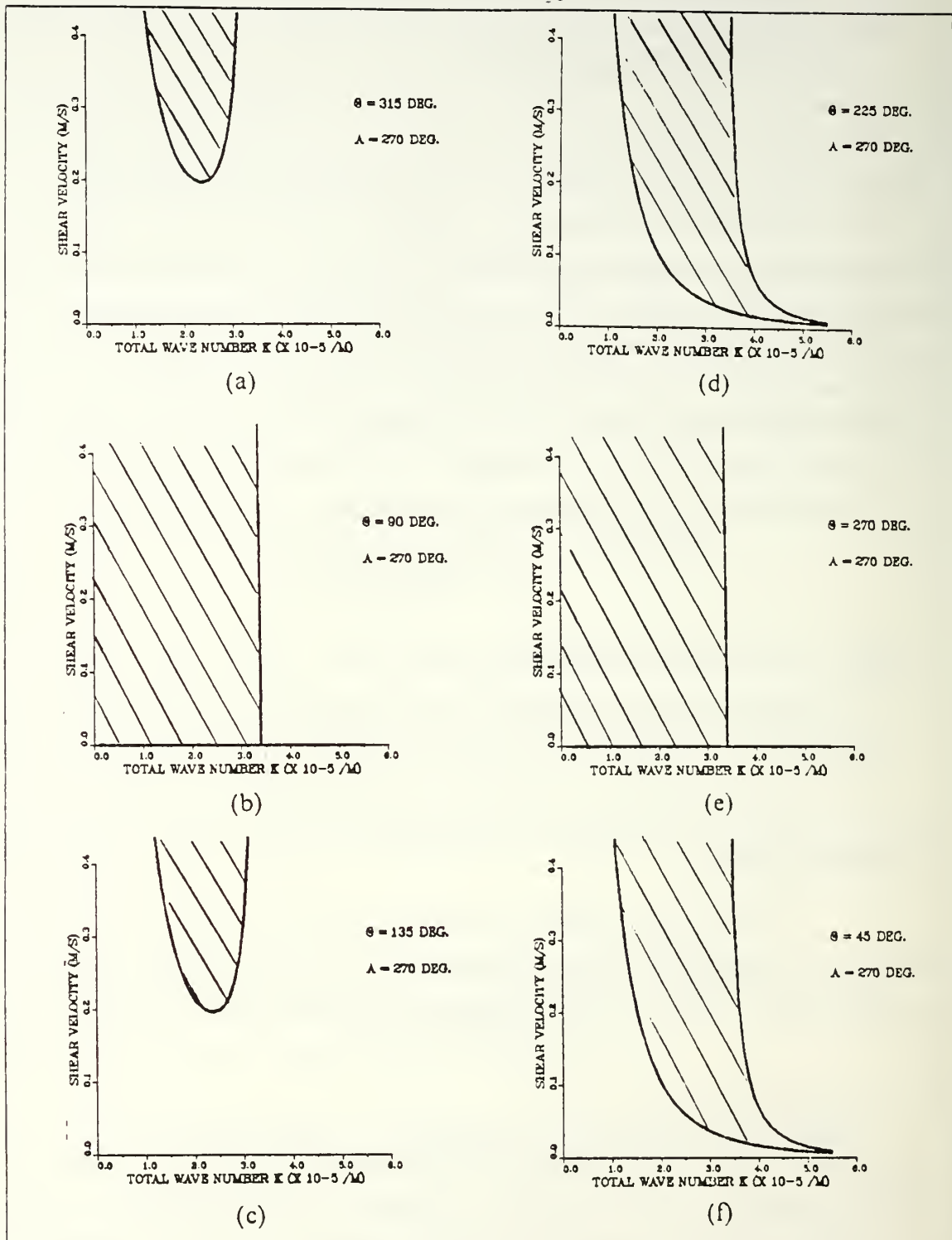


Figure 3.2 Marginal Stability Curves for $\alpha = 270^\circ$.

Curves for θ of (a) 45° , (b) 90° , (c) 135° , (d) 225° , (e) 270° and (f) 315° .

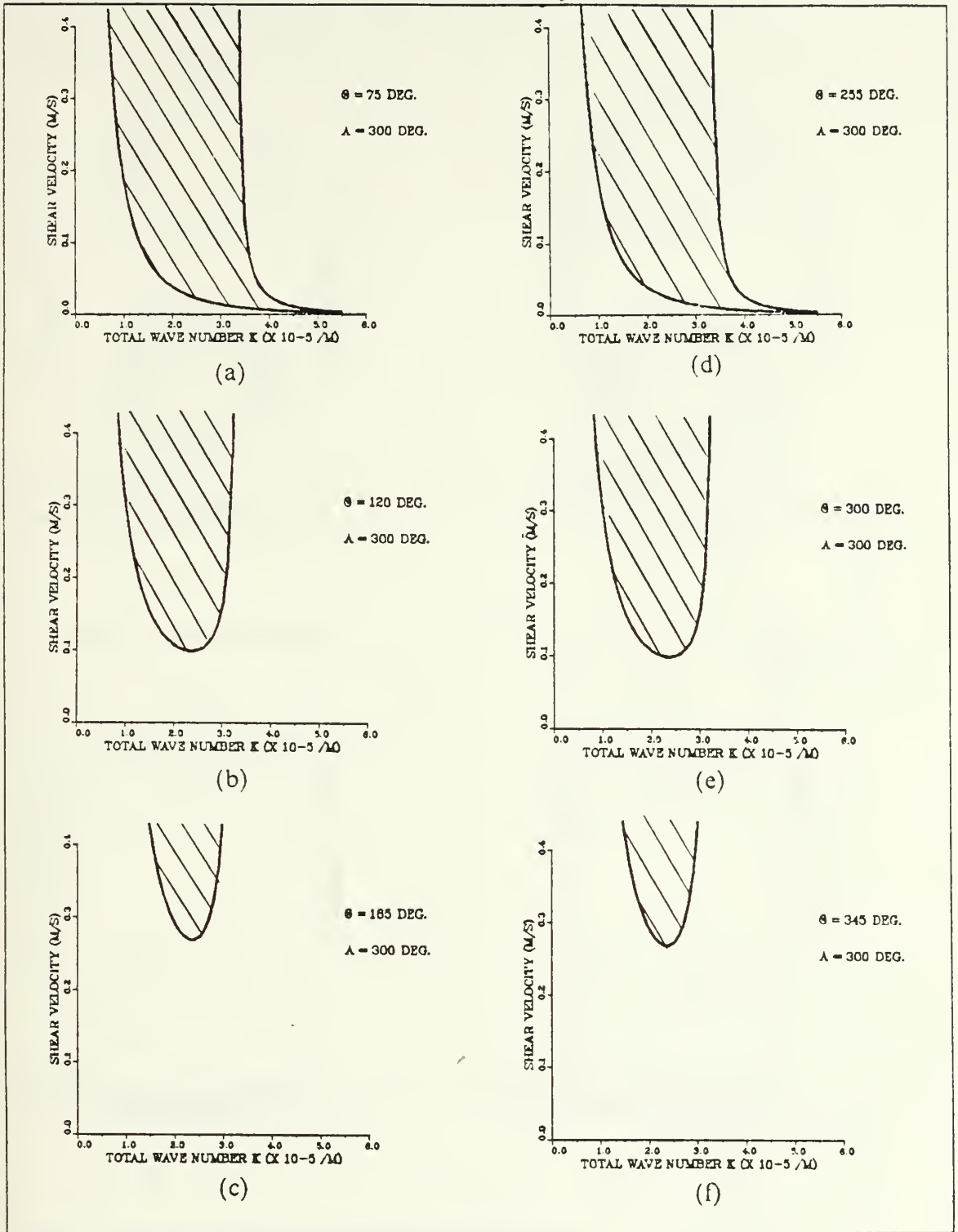


Figure 3.3 Marginal Stability Curves for $\alpha = 300^\circ$.

Curves for θ of (a) 75° , (b) 120° (c) 165° , (d) 255° , (e) 300° and (f) 345° .

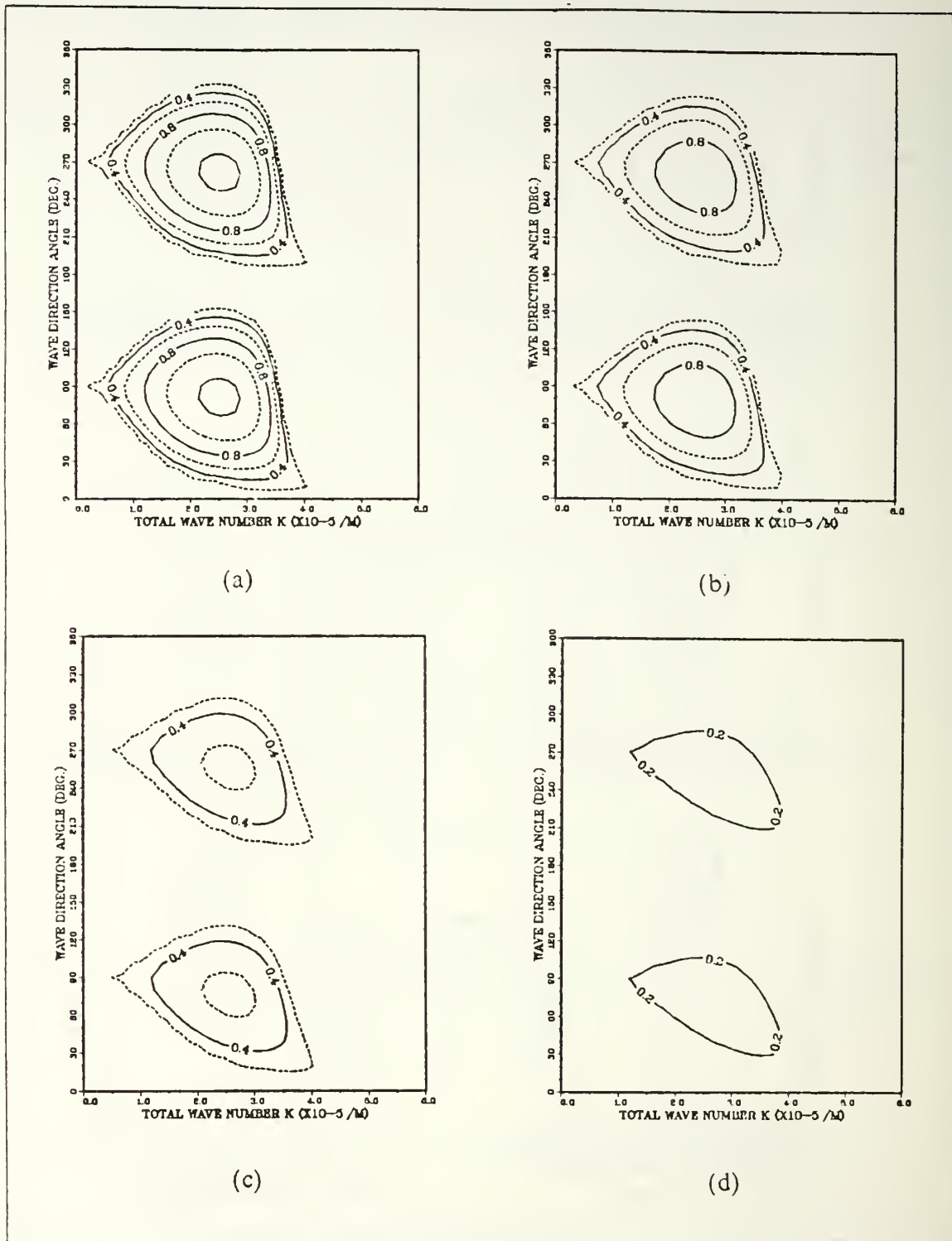


Figure 3.4 Growth Rates for $\alpha = 270^\circ$.

Growth rates ($\times 10^{-6} \text{ s}^{-1}$) for velocity shears of (a) 0.4, (b) 0.3, (c) 0.2 and (d) 0.1 m/s.

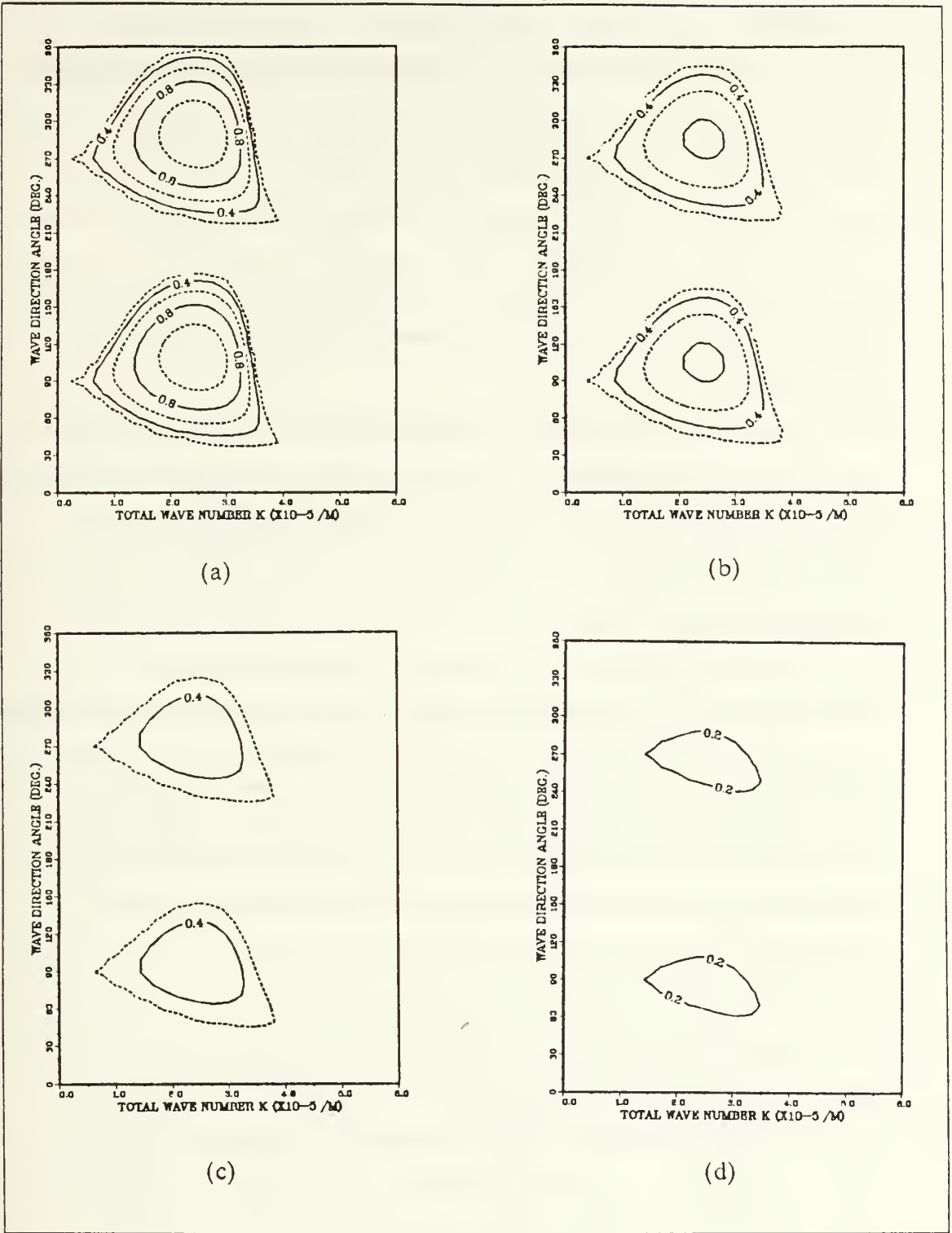


Figure 3.5 Growth Rates for $\alpha = 300^\circ$.

Growth rates ($\times 10^{-6} \text{ s}^{-1}$) for velocity shears of (a) 0.4, (b) 0.3, (c) 0.2 and (d) 0.1 m/s.

which would correspond to the fastest growing wave, occurs at different $\mathbf{K}-\theta$ intersections in each different shear flow case. This means the shear flow not only affects the magnitude of the growth rate but also the direction and wavenumber of the perturbation wave. As a result, any variation in the external forcing which is producing the shear flow would cause major alterations to the fastest growing wave. Another interesting point is that the growth rates for $\alpha = 270^\circ$ are higher in all shear conditions than for $\alpha = 300^\circ$ although the $\theta-\mathbf{K}$ plane positive growth rate areal extent is smaller. From the marginal stability curves, it is apparent that a meridional flow could have perturbations for which any non-zero shear would support instability. As a result, the additional claim that meridional flow yields the largest growth rate for a given shear can be made.

B. APPLICATION OF ANALYTIC RESULTS TO MODEL OUTPUT

The instability problem has now been formulated to approximate the numerically modeled situation. The next step is to examine the instabilities present in the model output fields as noted in section II.B.2 in terms of the previous section's results. If there are no inconsistencies, then the instabilities are most likely due to baroclinic instability of the basic flow.

From section II.B.2, it is obvious that there is a similarity of the output fields with respect to apparent wave-like structures. Not only do the same features appear in most of the runs, but their shape, direction and magnitudes are also similar. Table 3 shows the average values of relevant parameters from the model runs (where observed) for days 10, 20 and 30 for flow direction of $\alpha = 270^\circ$. Table 4 shows the same parameters for flow direction of $\alpha = 300^\circ$. The wave data for both tables was taken from model runs where the shear flow was close to 0.4 m/s (± 0.01 m/s).

TABLE 3
WAVE PARAMETERS FROM MODEL OUTPUT FIELDS ($\alpha = 270^\circ$)

DAY	θ (deg.)	\mathbf{K} (m^{-1})	L (km)
10	215	2.0×10^{-5}	310.0
20	249	2.6×10^{-5}	240.0
30	255	3.1×10^{-5}	200.0

TABLE 4
WAVE PARAMETERS FROM MODEL OUTPUT FIELDS ($\alpha = 300^\circ$)

DAY	θ (deg.)	K (m^{-1})	L (km)
10	238	2.3×10^{-5}	275.0
20	260	3.0×10^{-5}	209.0
30	269	3.2×10^{-5}	198.0

These days were selected because they represent the appearance (day 10), the growth (day 20) and the maturity (day 30) of the waves. By mapping the wave data from Tables 3 and 4 onto instability plots from section III.A.2, an evaluation of their relationship to the analytically derived baroclinic wave characteristics can be made.

Marginal stability curves are shown in Figure 3.6 for the flow angles and wave angles noted in Tables 3 and 4. The wavenumbers for those angle values are indicated and marked by the day the data is associated with at its intersection with the $V_s = 0.4$ m/s line. Of note is the fact that all of the plots show the waves within the unstable region for baroclinic instability. Additionally, as the waves shift in wavenumber towards shorter wavelengths, their shear excess increases to its maximum where the wave meets the asymptote corresponding to Equation 3.19.

Growth rate plots are shown in Figure 3.7 for velocity shears of 0.4 m/s. The parameter positions corresponding to days 10, 20 and 30 from Tables 3 and 4 are indicated to show the path the waves took as they developed. From Figure 3.7 it is apparent that the model output waves fall in the regions of positive growth rate but do not fall on or near the peak growth rate which would correspond theoretically to the position of the fastest growing wave. Also, the growth rate is low at day 10, reaches a maximum at day 20 and is decreasing by day 30. It must be kept in mind that these growth rates represent the analytic values given the wavelength and wave direction of the model output waves. They are not necessarily the same as the growth rates of the actual waves in the model output. The basic effect of the growth rate is to increase the amplitude of the growing wave in the following manner:

$$A = A_0 e^{(kc_1 t)} \quad (3.21)$$

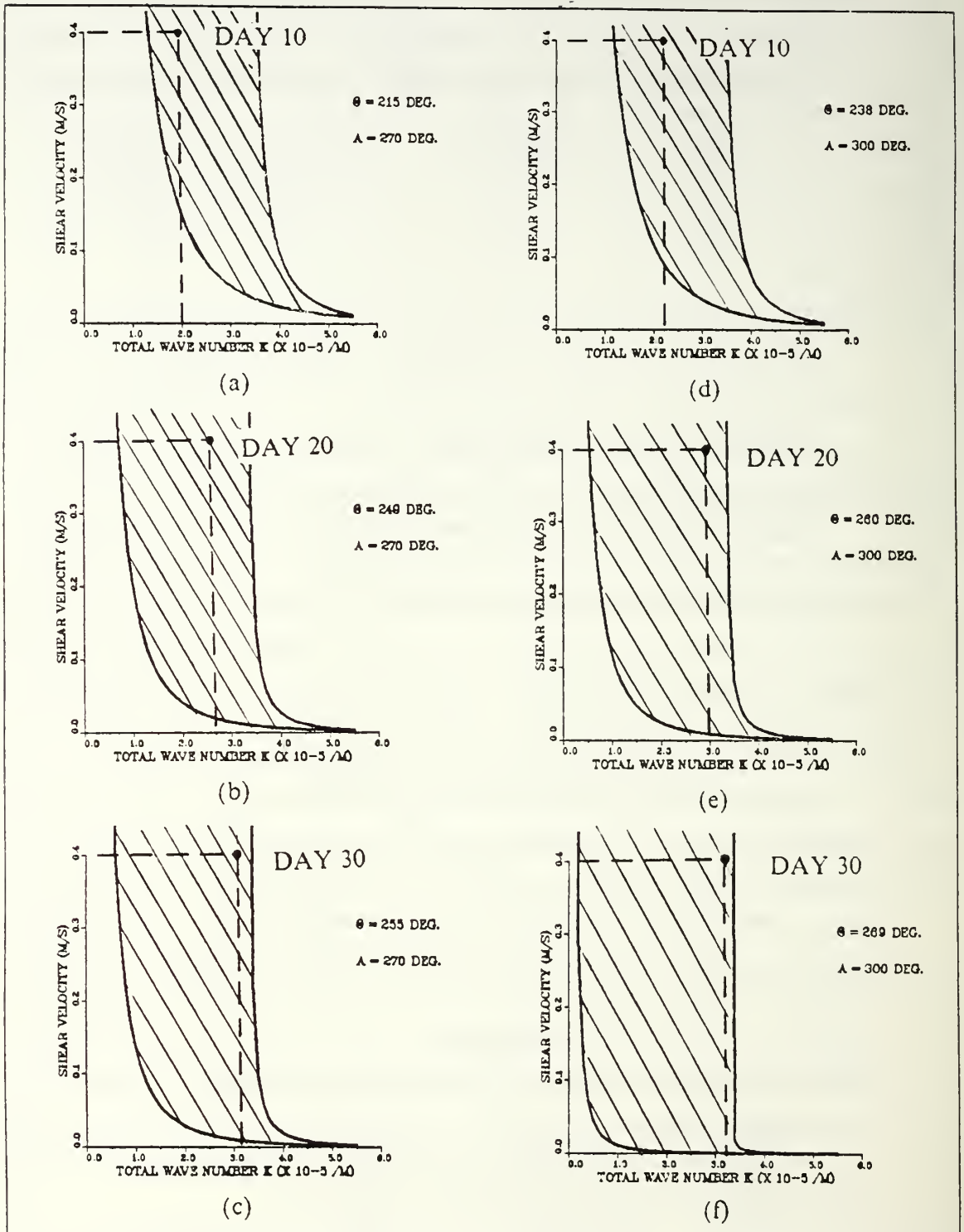


Figure 3.6 Marginal Stability Curves for Model Output Wave Characteristics.

Curves for $\alpha = 270^\circ$ and $\theta =$ (a) 215° , (b) 249° , (c) 255° and for $\alpha = 300^\circ$ and $\theta =$ (d) 238° , (e) 260° , (f) 269° .

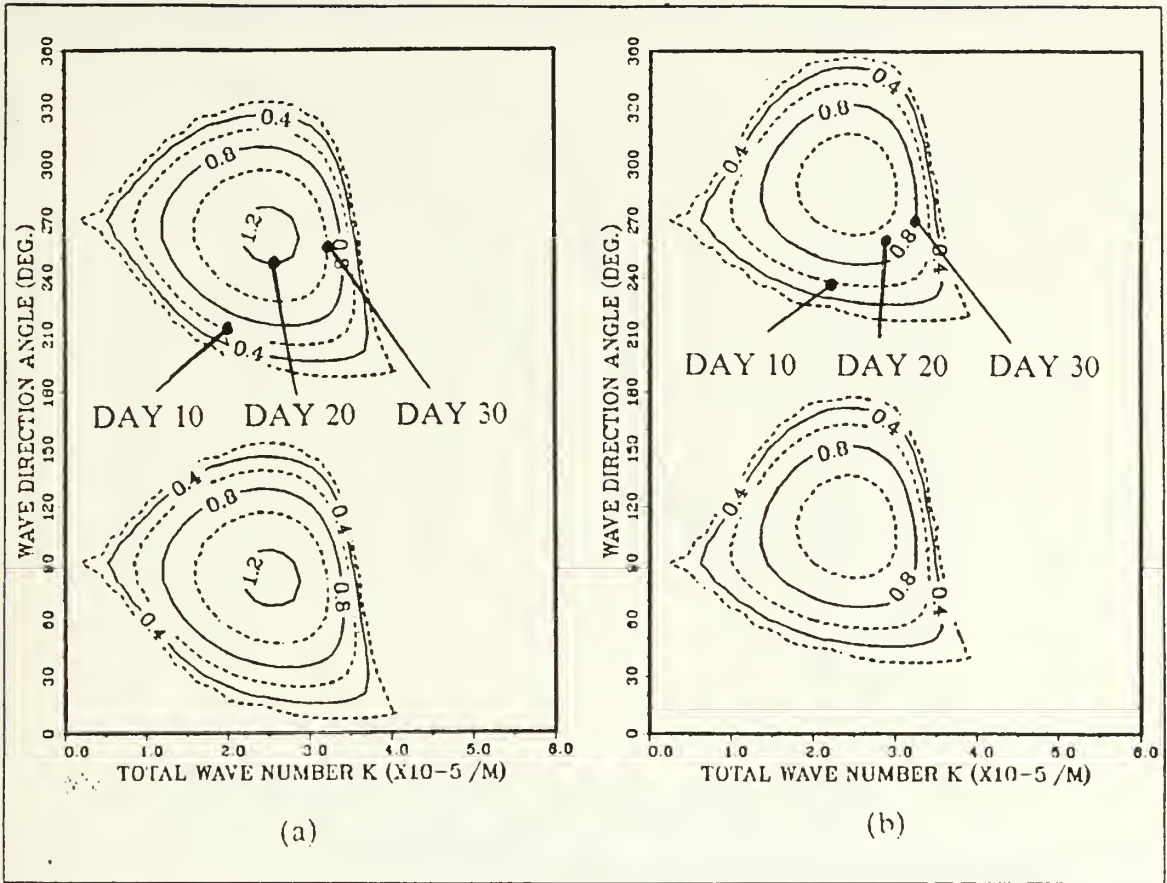


Figure 3.7 Growth Rate Positions of Model Output Waves for Shear Velocity of 0.4 m/s.

Parameter data from (a) Table 3 and (b) Table 4 plotted on growth rate ($\times 10^{-6} \text{ s}^{-1}$) fields from Figures 3.4.a and 3.5.a.

where A is the time varying amplitude and A_0 is the initial amplitude. Rearranging Equation 3.21,

$$\ln(A - A_0) = kc_1 t \quad (3.22)$$

yields an expression of the form, $y = mx$ where m represents the slope (kc_1). By plotting the natural log of the amplitude difference from the initial versus time, the growth rate can then be determined by the slope of the curve. Figure 3.8 shows the amplitude changes of the reference state waves during the model run.

Immediately apparent is the fact that the growth rate varies with time. It is low at first and grows to a maximum and then decreases. The information from Figure 3.8

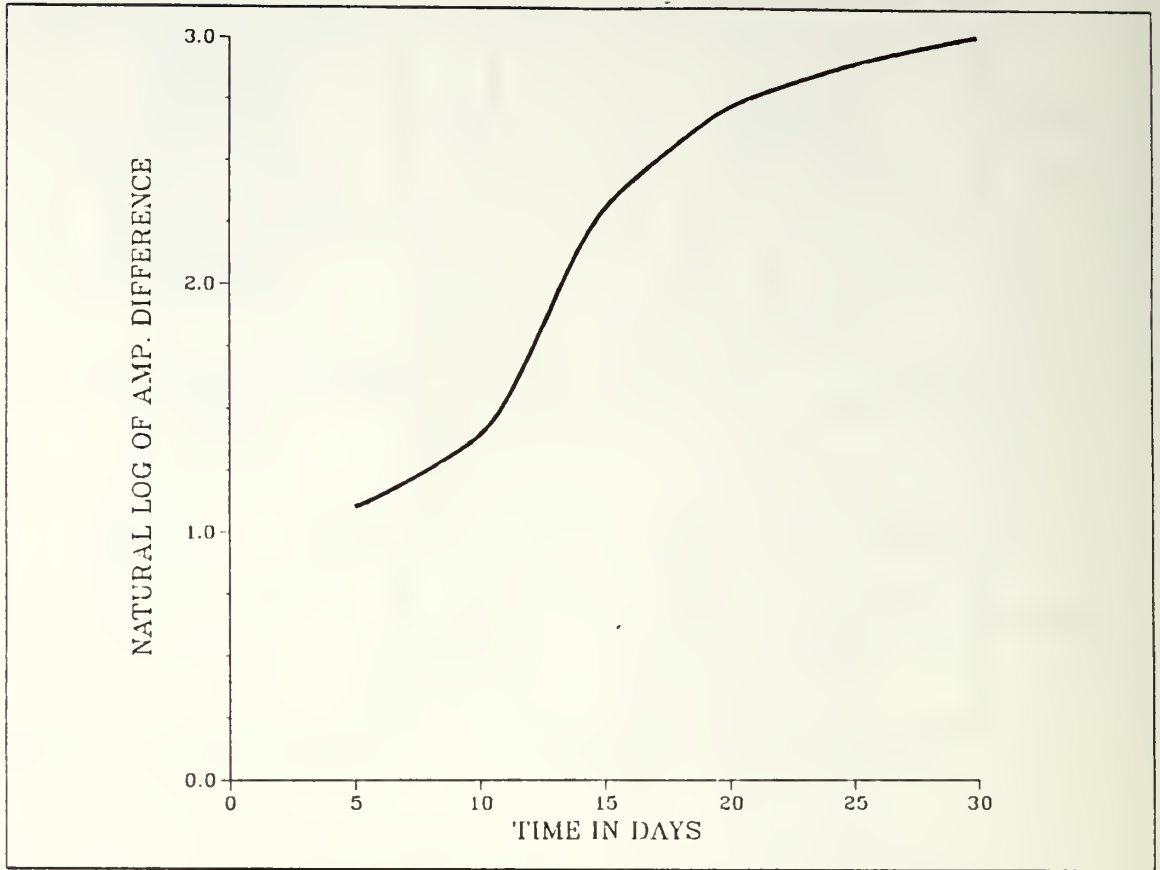


Figure 3.8 Reference State Wave Amplitude Growth.

can be easily converted into a plot of growth rate versus time. This is shown in Figure 3.9. The temporal variation of the growth rate is more clear and shows similar form to the growth rate progression observed in Figure 3.7.a.

Experiments 7 and 8 involved zonal flows. These were not meant to simulate the CCS but to evaluate the model response against theory. For a zonal flow, the wave growth must offset one hundred percent of the stabilizing planetary vorticity gradient, whereas for a meridional flow the gradient's effects are zero due to the $\beta \cos \theta$ term. Figure 3.10 shows the marginal stability curves for an eastward and westward zonal jet. The curves are not for any specific θ because the θ dependence cancels out of equation 3.18 for a zonal flow. Immediately apparent is the fact that the easterly jet should be more stable than the westerly jet since it has a much higher minimum shear velocity. This agrees with the experimental results where the easterly jet remained stable through the entire run and the westerly jet developed slight instabilities. Based on the curves

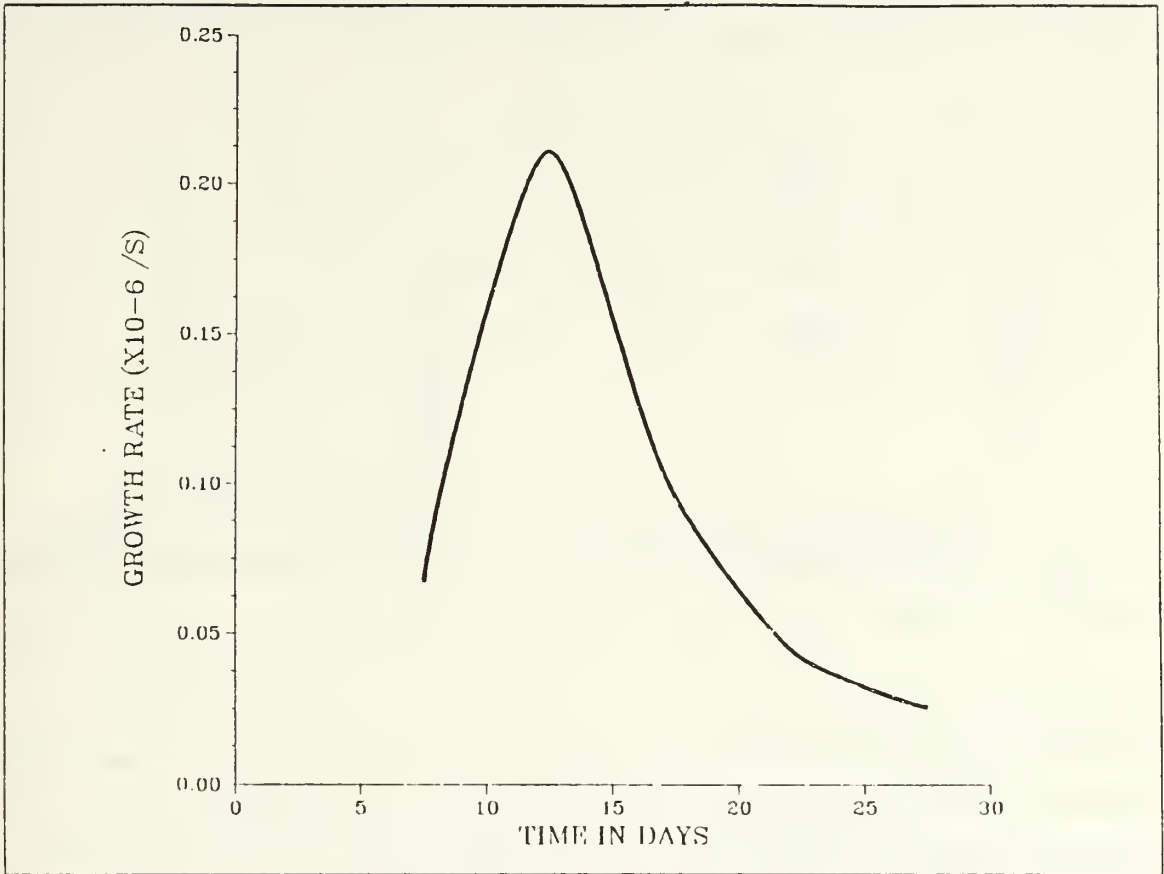


Figure 3.9 Growth Rate Variations of Reference State Waves.

for the zonal flow coupled with the fact that the shear velocity was 0.4 m/s, one might expect instability wave growth for both zonal flows similar to the reference run although this was not observed. The increase in the required V_{sc} for the zonal flows due to the β effect cuts down on the excess shear available for growth and apparently this excess is not quite great enough for wave growth. This points to frictional effects and will be discussed in the next section.

C. FURTHER ASPECTS OF THE INSTABILITY PROBLEM

The assumptions made to support the application of baroclinic instability theory to the numerical model results were necessary for any quantitative analysis to be made. Generally, there was very good agreement between linear instability theory and the model output which supports the contention that baroclinic instability is in fact the dominant dynamical process in the model and in the CCS. Nevertheless, there were discrepancies between the model simulations and the analytic predictions and these need to be addressed.

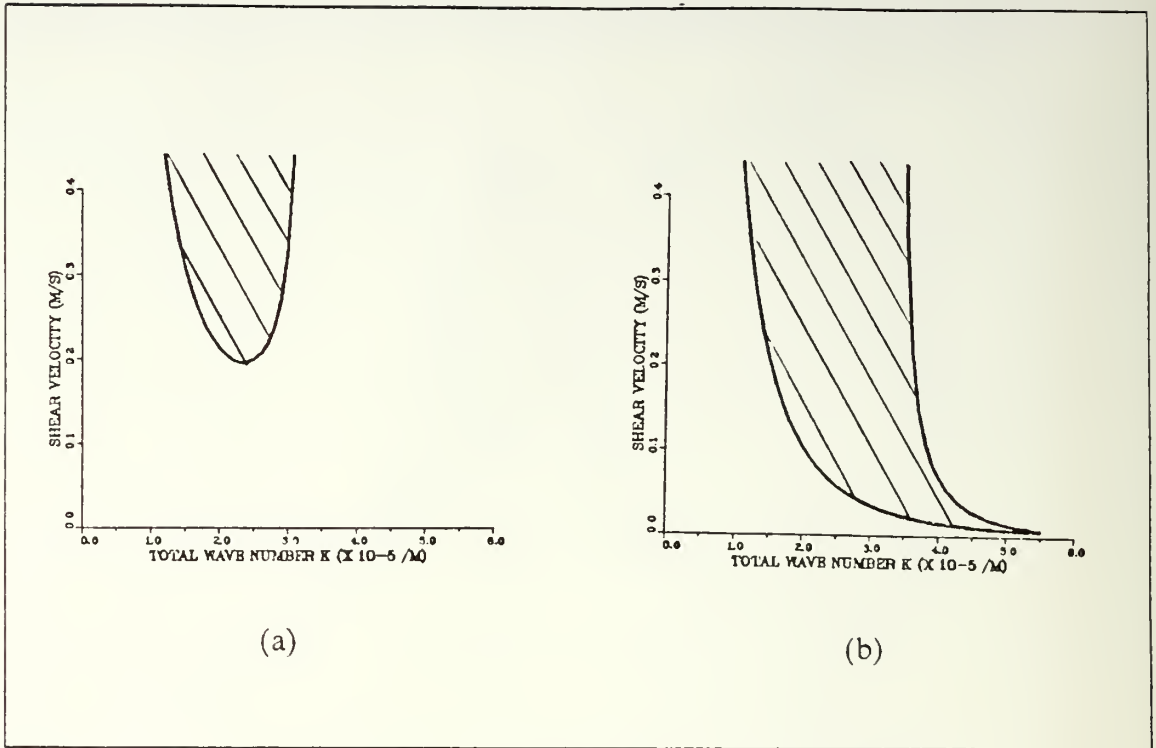


Figure 3.10 Marginal Stability Curves for Zonal Flow.

Curves are for $\alpha = 270^\circ$ and flows to (a) east and (b) west.

1. Effects of Friction

Without friction, the vertical phase shift of a baroclinic wave opposite the vertical velocity shear is an indication that $c_i > 0$ and the wave should grow (Pedlosky, 1979). However, when frictional forces are introduced, the wave can take on the same phase shift opposite the velocity shear and still be neutral. Instead of supplying energy for wave growth, the extracted energy is spent offsetting dissipation. Thus, in order to grow in the presence of friction, the baroclinic wave must have a greater phase shift than would be the case without friction. Since there is a maximum phase shift associated with maximum energy extraction, the growth rate of a baroclinic wave with friction should be less than that for a wave without friction.

In Figures 3.4 and 3.5 it was observed that changes in the shear velocity resulted in maximum growth rate value and θ - K positional changes. Frictional forces would tend to reduce the available energy for growth which is equivalent to a reduction

in the shear velocity. For this reason, the numerical output waves could not be expected to fall on the maximum growth rate parametric positions predicted by the non-frictional analytic development. Another complicating factor is the way in which friction was parameterized in the numerical model. By using a $A_h \nabla^2 V$ form, friction is a strong function of the velocity field. Since the velocity field in the domain changed drastically as the baroclinic waves developed, the frictional forcing must also have changed drastically. Thus, the frictional alteration of the maximum growth rate θ - K position would take on temporal variability. This might explain one reason the model output waves were observed to vary in wavenumber and direction through the model runs.

2. Non-linear Instability Effects

In linear instability theory the perturbation wave is unbounded as long as it meets the necessary conditions for instability which are defined in terms of the basic state. Obviously, this is not realistic as the waves grow to finite amplitude. Non-linear theory explains how advection affects the wave growth.

As Pedlosky (1979) pointed out, it is the basic state in the absence of the perturbation wave that must be used as criterion for instability vice any instantaneous flow profile. Variations in the flow profile as the wave develops, however, does have an effect on the wave. When the wave reaches a point where the instantaneous mean flow would not support instability, the wave growth rate is at its maximum and will start to decline. Although declining, the growth rate is still positive and the wave is still growing even though the instantaneous mean flow might support no instability. The change in growth rate is accompanied by a reduction of the phase shift of the wave in the vertical until growth is stopped as the phase shift reaches zero. The process does not stop here but continues into the phase orientation that causes wave decline. As with the growth, the decline will hit a maximum and reverse and the whole process of growth and decay will oscillate back and forth (Pedlosky, 1979). Thus, the variations in the wave growth rate observed in Figure 3.9 and inferred from Figure 3.7 could well be indicative of non-linear effects present in the model and presumably, the CCS.

When considering the effects of friction, variations in the available energy to the wave were correlated to variations in the parametric characteristics of the maximum growth wave. Non-linear theory predicts similar variations in the available energy due to the changes in the mean flow brought about by the perturbation wave.

Hence, it is another possible causative factor for the model output, since the model is non-linear, to exhibit variability in baroclinic wave wavenumber and direction over time.

3. Mixed Instability Effects

Most treatments of the instability problem are either focused on baroclinic or barotropic instability. In the CCS and the numerical model, flows have both horizontal and vertical shears. It was assumed in the analytic development of the baroclinic instability problem in section III.A.1 that barotropic instability was not the dominant instability process based on the scales of the observed disturbances. However, it may be that barotropic instability does have a slight influence on the baroclinically unstable waves.

Pedlosky (1979) showed that for a system with vertical and horizontal velocity shears, the characteristics of the most unstable wave can only be derived with exhaustive calculation given a detailed spatial distribution of velocity and potential vorticity. Changing the parameters of the flow can have a strong impact on the type of instability present and the wavelength. It is believed that throughout the numerical simulations, baroclinic instability remained the dominant instability process but barotropic instability may have altered the characteristics of the fastest growing wave.

4. Baroclinic Instability with Complex Wavenumbers

In developing the baroclinic instability problem, a particular perturbation form was assumed. This form is common to nearly all studies of this type of instability and is shown by Equations 3.9 and 3.14. The crucial point is the selection of a real wavenumber and a complex phase speed.

Hogg (1976) examined analytically and numerically the baroclinic instability process in a zonal flow where the perturbation form allowed both complex phase speed and complex wavenumber. In general, his results indicated a wavenumber cutoff between spatially growing ($k_i > 0$) and temporally growing ($c_i > 0$) waves. Temporally growing waves were confined to long wavelengths while spatially growing waves were confined to the shorter wavelengths.

In a study of Gulf Stream meanders, Watts and Johns (1982) used statistical analysis of cross stream data and derived values for both temporal and spatial growth rates of the meanders. Contrary to Hogg (1976), Watts and Johns' (1982) results indicated that spatial and temporal growth rates can occur in similar wavelength regimes. Figure 3.11 shows the growth rate versus wavenumber relation for both spatial and temporal growth found by Watts and Johns (1982).

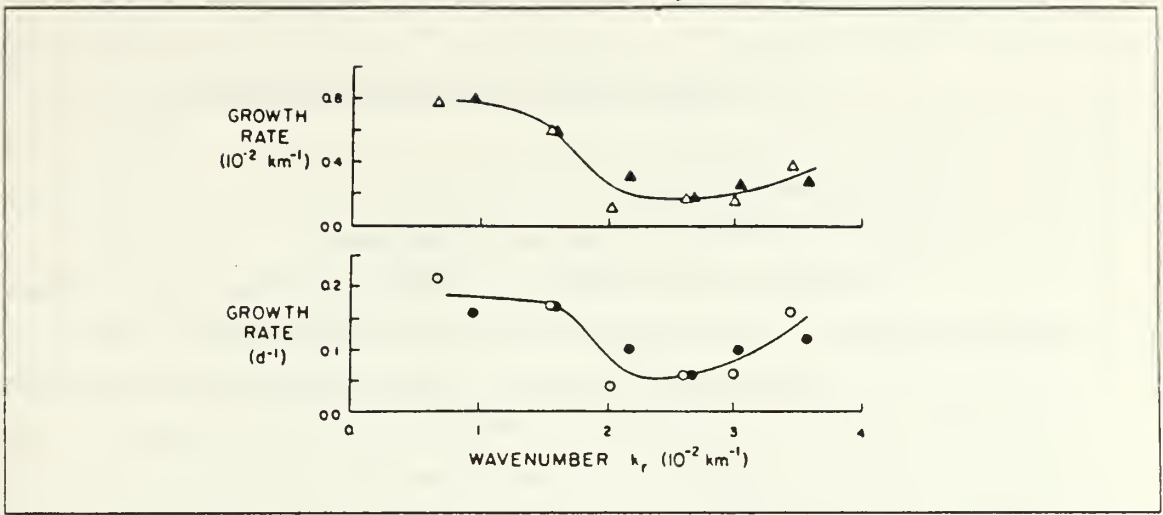


Figure 3.11 Spatial and Temporal Wave Growth of Gulf Stream Meanders (Watts and Johns, 1982).

There is evidence both analytically and observationally that spatial growth may be involved in the baroclinically unstable wave. Although Hogg (1976) concentrated on spatial growth ($k_i > 0$) and Watts and Johns (1982) observed only temporal and spatial growth ($c_i > 0, k_i > 0$), there is nothing in the theory that prevents a combination of temporal growth and spatial decline ($c_i > 0, k_i < 0$). This might also explain the variation in the observed wavelengths in the model output from long to short while the waves were growing in time.

IV. DISCUSSION AND CONCLUSIONS

A. ANALYSIS OF RESULTS

1. Comparison of Results with Observational Data

As mentioned in the introduction, filament structure, spatial distributions and temporal variabilities are well known. In order to validate the results of this study, there should be general agreement with the existing information and if discrepancies are present there should be some theoretical basis for the differences. In Table 5 values are shown for the range and magnitude of the observed versus the modeled characteristics. The value for the observed wavelength and direction is from Ikeda and Emery (1984) and the observed offshore extent is from Brink and Hartwig (1985). The rest of the observed values are from Flament *et al.* (1985).

TABLE 5
FILAMENT CHARACTERISTICS, OBSERVED VS. MODELED

PARAMETER	OBSERVED	MODELED
Wavelength	100-400 km	198-310 km
Wave Direction	~ 270°	215-269°
Off-shore Extent	100-500 km	100-800 km
Maximum Off-shore Velocity	~ 0.5 m/s	0.5 m/s
Maximum On-shore Velocity	~ 0.35 m/s	0.4 m/s
Growth rate (e-folding time)	~ 1-2 weeks	~ 10 d

It would seem that the only parameter that deviated significantly was the wave direction. The reason for this will be discussed in the next section. Otherwise the agreement strongly supports the contention that the modeled phenomena are in fact representative of filaments in the CCS.

2. The Filament Formation Process

The filament formation process is quite complex. Although baroclinic instability is clearly the dominant mechanism, there are other forces at work that cannot be neglected.

In the first phases of growth, the wave is affected by the east-west horizontal velocity shear. Close to the jet, the wave front is advected strongly to the south. Farther offshore, the jet effect on the wave propagation decreases due to the mean velocity gradient. This causes the wave vector direction to be deflected from the seemingly more favorable southerly direction to a near westerly direction. As the wave gains energy from the vertical shear of the mean flow, advection of the mean flow in a zonal direction starts to break down the east-west horizontal velocity shear and the wave direction rotates towards its more optimum direction and its wavelength shortens to maximize the growth rate. Non-linearities become dominant as the wave reaches such a magnitude that the instantaneous mean flow is stable and the wave growth starts to decline. This is as far as the waves were modeled, but it would be expected that the waves would go into an oscillatory growth-decline mode until damped by friction.

Obviously, this whole analysis is contingent on a constant wind stress forcing for periods on the order of months which is hardly realistic. It can be expected that constant forcing may persist for weeks at a time in which case the initial growth and development holds true.

From an observational standpoint, the filaments observed are nearly always oriented perpendicular to the flow indicating a southerly wave direction. This does not mean that the described theory of development is necessarily flawed, it just means that by the time the waves are observable, they have probably already twisted around into their more optimum configuration.

B. IMPORTANCE OF RESULTS

There have been numerous studies of zonal instability processes and a few of meridional situations but there is a large and distinct scarcity of studies of flows in-between. When one considers currents such as the Gulf Stream, the Kuroshio and, of course, the CCS which have flows that are not always east-west or north-south, it becomes evident that more attention should be placed on this discrepancy.

As demonstrated, the behavior of a flow that is non-zonal is dramatically different from a zonal flow. In a zonal flow, the energy releasing horizontal temperature gradient and the stabilizing planetary vorticity gradient are always working against each other. In a meridional flow, energy release can take place without any component of β acting on it; hence, any shear above the dissipation level may produce

instability. For the in-between case, the wave must assume a balance between the maximization of energy release and the dampening effects of the planetary vorticity gradient.

C. RECOMMENDATIONS FOR FUTURE STUDIES

There are several aspects of this modeling work that could be modified to better simulate the CCS. A better resolution model would help significantly to bring the barotropic instability process into view. This is particularly important to the filament situation since observational evidence has shown instabilities along the filament frontal region of the scale of R_d that are claimed to be the result of barotropic instability (Flament *et al.*, 1985). A model with more layers would give the vertical resolution necessary to properly simulate the CCS in all of its configurations, particularly its late summer profile of a strong southward surface jet and a poleward undercurrent all above a relatively quiescent deep water region. The addition of some temporal variability to the coastal jet strength would help to better understand wind stress variation effects on existing filaments and the growth of future filaments. Continued intensive *in situ* and satellite gathering of oceanographic data is vitally important to understanding the physical processes necessary to better reproduce the observed filament structures numerically. To thoroughly determine if baroclinic instability is occurring in the CCS, an elaborate experiment would have to be designed to resolve spatially and temporally the mesoscale motions. An experiment comparable to the POLYMODE experiment in the North Atlantic would be necessary.

D. CONCLUSIONS

Baroclinic instability is a prime generating force for filaments formed south of Cape Mendocino in the CCS. Barotropic instability along with non-linearities, frictional effects and possible spatial wave growth may help to modify the characteristics of the growing baroclinically unstable waves.

Filament growth is strongly dependent on the vertical velocity shear, the vertical structure and the mean flow direction. Any attempt to model filaments must carefully parameterize these quantities if accurate and thus useable results are to be obtained. Indeed, for any numerical simulation of currents with unknown instabilities, their values are crucial to correct simulations. Improper understanding of their spatial and temporal characteristics can seriously affect the validity of the model results.

APPENDIX

SYMBOLS AND NOTATION

A_h	Laplacian lateral friction coefficient	
A_n	Amplitude coefficient for normal mode solution for n^{th} layer	
c	Phase speed of perturbation wave	
$D(x,y)$	Variable depth of topography	
D_1	Upper layer thickness	
F_i	Froude number for i^{th} layer	$= f_0^2 L^2 / g' H_i$
f_0	Coriolis parameter for mean latitude	
g	Gravitational acceleration	
g'	Reduced gravitational acceleration	$= g(\rho_2 - \rho_1) / \rho_1$
h_i	Instantaneous layer thickness	
H_i	Upper ($i=1$) and lower ($i=2$) layer mean thickness	
\mathbf{k}	Unit vector in the z direction	
k	Perturbation wave number in the x direction	
ℓ	Perturbation wave number in the y direction	
K	Total wave number for perturbation wave	$= k^2 + \ell^2$
L	Horizontal scale length	
p_1	Pressure in the upper layer	$= g(h_1 + h_2 + d)$
p_2	Pressure in the lower layer	$= p_1 - g'h_1$
R_d	First internal Rossby radius of deformation	$= [g'H_1 H_2 / f_0^2 (H_1 + H_2)]^{1/2}$
R_0	Rossby number	$= U / fL$
U	Scale velocity	
u_i, v_i	Velocities in the x and y directions	
U_i, V_i	Transport in the x and y directions	
V_s	Shear velocity	$= (u_1^2 + v_1^2)^{1/2}$
V_{sc}	Critical shear velocity for instability	
x, y	Cartesian coordinates directed N and W respectively	
α	Angle mean flow vector makes with x axis	
β_0	Variation of Coriolis parameter with latitude	$= df/dy$
β	Scaled variation of Coriolis parameter with latitude	$= \beta_0 L^2 / U$
γ	Basin rotation angle from east	
$\Delta x, \Delta y$	Grid spatial resolution	

Δt	Model time increment	
θ	Angle perturbation wave vector makes with x axis	
Λ_i	Dimensionalized Froude number for i^{th} layer	$= F_i' L^2$
ρ_i	Density in i^{th} layer	
ρ_0	Mean density	
σ	Frequency of perturbation wave	
τ	Wind stress vector	
ϕ_i	Perturbation stream function for i^{th} layer	
Ψ_i	Basic state stream function for i^{th} layer	
ψ_i	Variable stream function for i^{th} layer	
∇	Gradient operator	$= \partial/\partial x + \partial/\partial y$
∇^2	Laplacian operator	$= \partial^2/\partial x^2 + \partial^2/\partial y^2$

LIST OF REFERENCES

- Batteen, Mary L., 1987: Model simulations of a coastal jet and undercurrent in the presence of eddies and jets in the California Current System. Submitted.
- Brink, K.H. and E.O. Hartwig, 1985: *Coastal Transition Zone Workshop Report*. Office of Naval Research, 67 pp.
- Camerlengo, A. and J.J. O'Brien, 1980: Open boundary conditions in rotating fluids. *J. Comput. Phys.*, **35**, 12-35.
- Chen, Ching-Yen, 1986: Topographic influences in the California Current System. M.S. thesis, Naval Postgraduate School, 49 pp.
- Flament, P., L. Armi, and L. Washburn, 1985: The evolving structure of an upwelling filament. *J. Geophys. Res.*, **90**, 11765-11778.
- Hickey, B.M., 1979: The California Current System - hypothesis and facts. *Prog. in Oceanogr.*, **8**, 191-279.
- Hogg, N.G., 1976: On spatially growing baroclinic waves in the ocean. *J. Fluid Mech.*, **78**, 217-235.
- Hurlburt, H.E., 1974: The influence of coastline geometry and bottom topography on the eastern ocean circulation. Ph.D. thesis, Florida State University, 103 pp.
- _____, and J.D. Thompson, 1980: A numerical study of Loop Current intrusions and eddy shedding. *J. Phys. Oceanogr.*, **9**, 1611-1651.
- _____, and _____, 1982: The dynamics of the Loop Current and shed eddies in a numerical model of the Gulf of Mexico. *Hydrodynamics of Semi-Enclosed Seas*, Elsevier, 243-298.
- Huyer, A., R.L. Smith and B.M. Hickey, 1984: Observations of a warm-core eddy off Oregon, January to March 1978. *Deep-Sea Res.*, **31**, 97-117.
- Ikeda, M. and W.J. Emery, 1984: Satellite observations and modeling in the California Current System off Oregon and northern California. *J. Phys. Oceanogr.*, **14**, 1434-1450.
- Kamenkovich, V.M., M.N. Koshlyakov and A.S. Monin, 1986: *Synoptic Eddies in the Ocean*. D. Reidel, 433 pp.
- Kosro, P.M. and A. Huyer, 1986: CTD and velocity surveys of seaward jets off northern California, July 1981 and 1982. *J. Geophys. Res.*, **91**, 7680-7690.
- _____, 1987: Structure of the coastal current field off northern California during the Coastal Ocean Dynamics Experiment. *J. Geophys. Res.*, **92**, 1637-1654.
- Mooers, C.N. and A.R. Robinson, 1984: Turbulent jets and eddies in the California Current and inferred cross-shore transport. *Science*, **223**, 51-53.

- Mysak, L.A., 1977: On the stability of the California Undercurrent off Vancouver Island. *J. Phys. Oceanogr.*, **7**, 904-917.
- _____, E.R. Johnson and W.W. Hsieh, 1981: Baroclinic and barotropic instabilities of coastal currents. *J. Phys. Oceanogr.*, **11**, 209-230.
- Owen, R.W., 1980: Eddies of the California Current System: Physical and ecological characteristics. *The California Islands*, D. M. Power, ed., Santa Barbara Museum of Natural History.
- Pedlosky, J., 1979: *Geophysical Fluid Dynamics*. Springer-Verlag, 624 pp.
- Rienecker, M.M., C.N.K. Mooers, D.E. Hagan, and A.R. Robinson, 1985: A cool anomaly off northern California: An investigation using IR imagery and *in situ* data. *J. Geophys. Res.*, **90**, 4807-4818.
- Smith, D.C., IV, and R.O. Reid, 1982: A numerical study of non-frictional decay of mesoscale eddies. *J. Phys. Oceanogr.*, **12**, 244-255.
- _____, and J.J. O'Brien, 1983: The interaction of a two layer isolated mesoscale eddy with topography. *J. Phys. Oceanogr.*, **13**, 1681-1697.
- _____, 1986: A numerical study of Loop Current eddy interaction with topography in the western Gulf of Mexico. *J. Phys. Oceanogr.*, **16**, 1260-1272.
- Stabeno, P.J. and R.L. Smith, 1987: Deep Sea Currents off Northern California. *J. Geophys. Res.*, **92**, 755-771.
- Watts, D.R. and W.E. Johns, 1982: Gulf Stream meanders: Observations on propagation and growth. *J. Geophys. Res.*, **87**, 9467-9476.

INITIAL DISTRIBUTION LIST

		No. Copies
1.	Defense Technical Information Center Cameron Station Alexandria, VA 22304-6145	2
2.	Library, Code 0142 Naval Postgraduate School Monterey, CA 93943-5002	2
3.	Chairman (Code 68Co) Department of Oceanography Naval Postgraduate School Monterey, CA 93943	1
4.	Chairman (Code 63Rd) Department of Meteorology Naval Postgraduate School Monterey, CA 93943	1
5.	Dr. D. C. Smith IV (Code 68Si) Department of Oceanography Naval Postgraduate School Monterey, CA 93943	2
6.	Dr. M. L. Batteen (Code 68Bv) Department of Oceanography Naval Postgraduate School Monterey, CA 93943	2
7.	Dr. R. L. Haney (Code 63Hy) Department of Oceanography Naval Postgraduate School Monterey, CA 93943	1
8.	LT David A. Olivier, USN 6209 Fushsimi Ct. Burke, VA 22015	2
9.	Director Naval Oceanography Division Naval Observatory 34th and Massachusetts Avenue NW Washington, DC 20390	1
10.	Commander Naval Oceanography Command NSTL Station Bay St. Louis, MS 39522	1

11. Commanding Officer 1
 Naval Oceanographic Office
 NSTL Station
 Bay St. Louis, MS 39522
12. Commanding Officer 1
 Fleet Numerical Oceanography Center
 Monterey, CA 93943
13. Commanding Officer 1
 Naval Ocean Research and Development Activity
 NSTL Station
 Bay St. Louis, MS 39522
14. Commanding Officer 1
 Naval Environmental Prediction Research Facility
 Monterey, CA 93943
15. Chairman, Oceanography Department 1
 U.S. Naval Academy
 Annapolis, MD 21402
16. Naval Ocean Research and Development Activity 1
 800 N. Quincy Street
 Arlington, VA 22217
17. Office of Naval Research (Code 420) 1
 800 N. Quincy Street
 Arlington, VA 22217
18. Scientific Liaison Office 1
 Office of Naval Research
 Scripps Institution of Oceanography
 La Jolla, CA 92037
19. Commander 1
 Oceanographic Systems Pacific
 Box 1390
 Pearl Harbor, HI 96860
20. Commanding Officer 1
 Naval Eastern Oceanography Center
 Naval Air Station
 Norfolk, VA 23511
21. Commanding Officer 1
 Naval Western Oceanography Center
 Box 113
 Pearl Harbor, HI 96860
22. Commanding Officer 1
 Naval Oceanography Command Center, Rota
 Box 31
 FPO San Francisco, CA 09540

23. Commanding Officer 1
Naval Oceanography Command Center, Guam
Box 12
FPO San Francisco, CA 96630
24. Program Director 1
Physical Oceanography
National Science Foundation
Washington, DC 20550
25. Dr. C. N. K. Mooers 1
Institute for Naval Oceanography
Room 311, Bldg 1100
NSTL Station
Bay St. Louis, MS 39529
26. Chung-Ming Fang 1
Chinese Naval Hydrographic and Oceanographic Office
Tsoying, Kaohsiung
Taiwan 813
Republic of China

18767 3

Thesis
0465 Olivier
c.1 Numerical simulations
of the California Cur-
rent: filament formation
as related to baroclinic
instability.

15 AUG 90

35547

Thesis
0465 Olivier
c.1 Numerical simulations
of the California Cur-
rent: filament formation
as related to baroclinic
instability.

thesO465

Numerical simulations of the California



3 2768 000 75461 8

DUDLEY KNOX LIBRARY